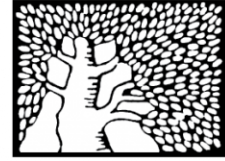


מכון ויצמן למדע

WEIZMANN INSTITUTE OF SCIENCE



Cxcl10(+) monocytes define a pathogenic subset in the central nervous system during autoimmune neuroinflammation

Document Version:

Accepted author manuscript (peer-reviewed)

Citation for published version:

Giladi, A, Wagner, LK, Li, H, Doerr, D, Medaglia, C, Paul, F, Shemer, A, Jung, S, Yona, S, Mack, M, Leutz, A, Amit, I & Mildner, A 2020, 'Cxcl10(+) monocytes define a pathogenic subset in the central nervous system during autoimmune neuroinflammation', *Nature Immunology*, vol. 21, no. 5, pp. 525-534.
<https://doi.org/10.1038/s41590-020-0661-1>

Total number of authors:

13

Digital Object Identifier (DOI):

[10.1038/s41590-020-0661-1](https://doi.org/10.1038/s41590-020-0661-1)

Published In:

Nature Immunology

License:

Other

General rights

@ 2020 This manuscript version is made available under the above license via The Weizmann Institute of Science Open Access Collection is retained by the author(s) and / or other copyright owners and it is a condition of accessing these publications that users recognize and abide by the legal requirements associated with these rights.

How does open access to this work benefit you?

Let us know @ library@weizmann.ac.il

Take down policy

The Weizmann Institute of Science has made every reasonable effort to ensure that Weizmann Institute of Science content complies with copyright restrictions. If you believe that the public display of this file breaches copyright please contact library@weizmann.ac.il providing details, and we will remove access to the work immediately and investigate your claim.



Cxcl10⁺ monocytes define a pathogenic subset in the central nervous system during autoimmune neuroinflammation

Amir Giladi^{1,6}, Lisa Katharina Wagner^{2,6}, Hanjie Li¹, Dorothea Dörr², Chiara Medaglia¹, Franziska Paul¹, Anat Shemer¹, Steffen Jung¹, Simon Yona³, Matthias Mack⁴, Achim Leutz^{2,5}, Ido Amit^{1,6} and Alexander Mildner^{2,6}

Multiple sclerosis (MS) is characterized by pathological inflammation that results from the recruitment of lymphoid and myeloid immune cells from the blood into the brain. Due to subset heterogeneity, defining the functional roles of the various cell subsets in acute and chronic stages of MS has been challenging. Here, we used index and transcriptional single-cell sorting to characterize the mononuclear phagocytes that infiltrate the central nervous system from the periphery in mice with experimentally induced autoimmune encephalitis, a model of MS. We identified eight monocyte and three dendritic cell subsets at acute and chronic disease stages in which the defined transcriptional programs pointed toward distinct functions. Monocyte specific cell ablation identified *Cxcl10*⁺ and *Saa3*⁺ monocytic subsets with a pathogenic potential. Transfer experiments with different monocyte and precursor subsets indicated that these *Cxcl10*⁺ and *Saa3*⁺ pathogenic cells were not derived from *Ly6C*⁺ monocytes, but from early myeloid cell progenitors. These results suggest that blocking specific pathogenic monocytic subsets, including *Cxcl10*⁺ and *Saa3*⁺ monocytes, could be used for targeted therapeutic interventions.

Two main populations of monocytes have been described in most mammalian species¹. Mouse *Ly6C*⁻ monocytes (or *CD14*^{lo}*CD16*^{hi} monocytes in humans) patrol blood vessels and orchestrate the removal of damaged endothelial cells². Mouse *Ly6C*⁺ monocytes (or human *CD14*^{hi}*CD16*^{lo} monocytes) are equipped with chemokine receptors that allow their egression from the circulation into various tissues, where they can give rise to a large variety of monocyte-derived cells with distinct functions³. The idea that circulating *Ly6C*⁺ monocytes can differentiate into various cell subsets was challenged by single-cell analysis, which pointed out the cellular heterogeneity of *Ly6C*⁺ monocytes⁴ and the existence of different *Ly6C*⁺ monocyte subsets with potentially distinct, predetermined functions⁵. Specifically, *Ly6C*⁺ monocytes preferentially differentiated into iNOS-producing monocyte-derived cells during *Listeria* infection, while *Ly6C*⁺*MHCII*⁺*Cd209a*⁺ monocytes acquired a dendritic cell (DC)-like phenotype after colony stimulating factor 2 (CSF2) or lipopolysaccharide (LPS) exposure⁵. Emergency generation of distinct monocyte subsets might depend on the inflammatory stimulus. Thus, it was proposed that LPS promotes the development of monocytes from granulocyte-monocyte progenitors (GMPs), while CpG DNA triggers monopoiesis from monocyte-dendritic cell progenitors (MDPs)⁶. These data, in conjunction with a recent report that shows that monocytes develop from GMPs rather than from MDPs under physiological conditions⁷, indicate that our understanding of monopoiesis is incomplete.

MS and its model in mice, experimental autoimmune encephalomyelitis (EAE), are autoimmune disorders in which autoreactive T cells recognize myelin peptides and infiltrate the

central nervous system (CNS). Monocytes expressing the chemokine receptor CCR2 were identified as main drivers of EAE pathogenesis. Genetic depletion of CCR2⁺ monocytes leads to resistance to EAE, while the antibody-mediated depletion of monocytes reduces clinical symptoms in mice^{8–10}. CSF2 also critically contributes to the development of pathological myeloid cells^{11,12}. *Ly6C*⁺ monocyte-derived cells gain expression of *CD11c* (encoded by *Itgax*) and MHCII-related genes in the inflamed CNS. This has been interpreted as a sequential differentiation program⁹ but, alternatively, different monocyte subsets could give rise to distinct progeny on infiltration.

Here, we have characterized the cellular composition of mononuclear phagocytes infiltrating the inflamed spinal cord in mice with EAE by massively parallel single-cell RNA-seq (MARS-seq)¹³. We analyzed the acute and chronic stages of the disease and identified several molecularly distinct myeloid cell subsets. Some of these subsets were restricted to either the acute or chronic phase, supporting the idea that monocyte subsets can differentiate locally from one subset to the other as suggested previously^{14,15}. By taking advantage of a peripheral monocyte depletion strategy⁸, we identified two transcriptionally related monocyte subsets, namely *Cxcl10*⁺ and *Saa3*⁺ cells, with pathogenic potential in the spinal cord. Depletion of these cells correlated with reduced clinical symptoms. These subsets were mainly derived from monocytic precursor cells, and were independent of classical *Ly6C*⁺ monocytes. These results define a molecular road map of myeloid subset differentiation in MS pathogenesis, and may help unveil precise molecular avenues to modulate myeloid pathogenesis in the CNS.

¹Department of Immunology, Weizmann Institute of Science, Rehovot, Israel. ²Max-Delbrück-Center for Molecular Medicine (MDC), Berlin, Germany.

³Faculty of Dental Medicine, Hebrew University, Jerusalem, Israel. ⁴Department of Nephrology, Universitätsklinikum Regensburg, Regensburg, Germany.

⁵Institute of Biology, Humboldt University of Berlin, Berlin, Germany. ⁶These authors contributed equally: Amir Giladi, Lisa Katharina Wagner, Ido Amit,

Alexander Mildner. ✉e-mail: ido.amit@weizmann.ac.il; alexander.mildner@mdc-berlin.de

Results

Mononuclear phagocyte diversity in the inflamed CNS. To investigate the mononuclear phagocyte diversity in MS, we immunized wild-type C57Bl/6 mice with myelin oligodendrocyte glycoprotein peptide (MOG₃₅₋₅₅) to induce EAE. Animals were analyzed during the acute phase (day 16 postimmunization (PI); mean EAE score 2.9) and the chronic phase (day 30 PI; mean EAE score 2.2) of the disease (Fig. 1a). To specifically profile negative hematopoietic stem-cell-derived mononuclear phagocytes, we sorted CD11b⁺ cells, and excluded Ly6G⁺ cells (neutrophils) and CX₃CR1^{hi}CD44^{lo} cells (microglia¹⁶) (Fig. 1b). We combined MARS-seq¹³ with single-cell index sorting of Ly6C and MHCII to simultaneously measure the transcriptional and protein expression of individual cells. Analysis of 2,925 cells that passed the quality control (Extended Data Fig. 1) divided the data into 55 groups of cells (metacell)^{17,18}. A direct comparison of the metacell results with other algorithms such as Seurat¹⁹ indicated a high concordance between the clusters (Extended Data Fig. 2a). To assign metacells to distinct cell types or activation states, we performed correlation analysis and identified ten broad transcriptional states, some of which were transcriptionally related (Fig. 1c,d and Extended Data Fig. 2b). Each of these ten transcriptionally distinct myeloid subsets showed a distinct gene expression program (Fig. 1e), as well as differences in the expression of Ly6C and MHCII surface proteins (Fig. 1f). *Ly6c2*⁺*Sell*⁺*Ccr2*⁺ cells were identified as the Ly6C⁺ monocyte subset, while *Nr4a1*⁺*Pparg*⁺ cells, detected at a much lower frequency, were identified as Ly6C⁻ monocytes (Fig. 1e and Extended Data Fig. 2c). Proliferation-associated genes such as *Mki67*, *Ccna2* and *Ccnb2* were specifically expressed in a fraction of Ly6C⁺ monocytes. We also identified a cluster of microglial cells that expressed *Fcrls*, *Sall1* and *Tmem119*, and a small cluster of classical DC (cDC) defined by expression of *Flt3*, *Xcr1* and *Zbtb46* (Fig. 1d,e). High expression of genes that belong to type I interferon (IFN) pathway such as *Ifit1*, *Ifit2*, *Ifit3*, *Usp18* and *Irf7* were evident in *Ifit2*⁺ monocytes (Fig. 1d,e). Most of the remaining cells (1,810 cells, 62%) exhibited expression patterns distinct from that of steady-state myeloid cells and did not conform to known monocyte or macrophage populations (Fig. 1d,e), suggesting the existence of alternative activation or differentiation states in the infiltrating mononuclear phagocytes. Two macrophage subsets expressed *Arg1*, *Apoc2* and *C1qb* and were designated as *Arg1*⁺ macrophages I and II. Another macrophage cluster was characterized by expression of *Nos2*, *Gpnmb*, *Arg1* and *Fabp5* and was defined as *Nos2*⁺ macrophages, while two populations that expressed inflammatory genes such as *Saa3*, *Plac8* and *Gbp2*, or *Cxcl9*, *Cxcl10* and *Il1b* were designated as *Saa3*⁺ and *Cxcl10*⁺ monocytes, respectively (Fig. 1e and Extended Data Fig. 2b). All monocyte or macrophage subsets equally expressed *Ccr2* and *Ly6c2*, while expression of *Cd74* transcripts was restricted to the *Arg1*⁺ and *Nos2*⁺ subsets (Fig. 1g). In contrast, *Csf2rb* (encoding the common signaling β chain of CSF2 receptor) was highly expressed in *Cxcl10*⁺ monocytes compared to the remaining cells (Fig. 1g). The complete list of gene expression for each metacell cluster can be found in Supplementary Table 1.

To gain more information on the functions of these subsets, we performed gene-ontology enrichment analysis on the 60 most differential expressed genes from each group (Extended Data Fig. 2d,e and Supplementary Table 2). We identified a strong pro-inflammatory and pathogenic signature, defined as 'positive regulation of cytokine production and response to IFN- γ and LPS' in the *Saa3*⁺ and *Cxcl10*⁺ monocyte clusters (Extended Data Fig. 2e). Type I IFN responses were specific to the *Ifit2*⁺ monocyte cluster, while Ly6C⁺ monocytes were enriched for nuclear division pathways (Extended Data Fig. 2e), in accordance with their expression of cell cycle genes. The remaining macrophage clusters, comprising *Arg1*⁺ and *Nos2*⁺ macrophages, as well as microglia, were enriched for receptor-mediated endocytosis, regulation of vasculature development, wound healing and tissue remodeling processes (Extended Data Fig. 2e). Our data indicate that at least ten molecularly distinct myeloid populations are present in the CNS of mice with EAE.

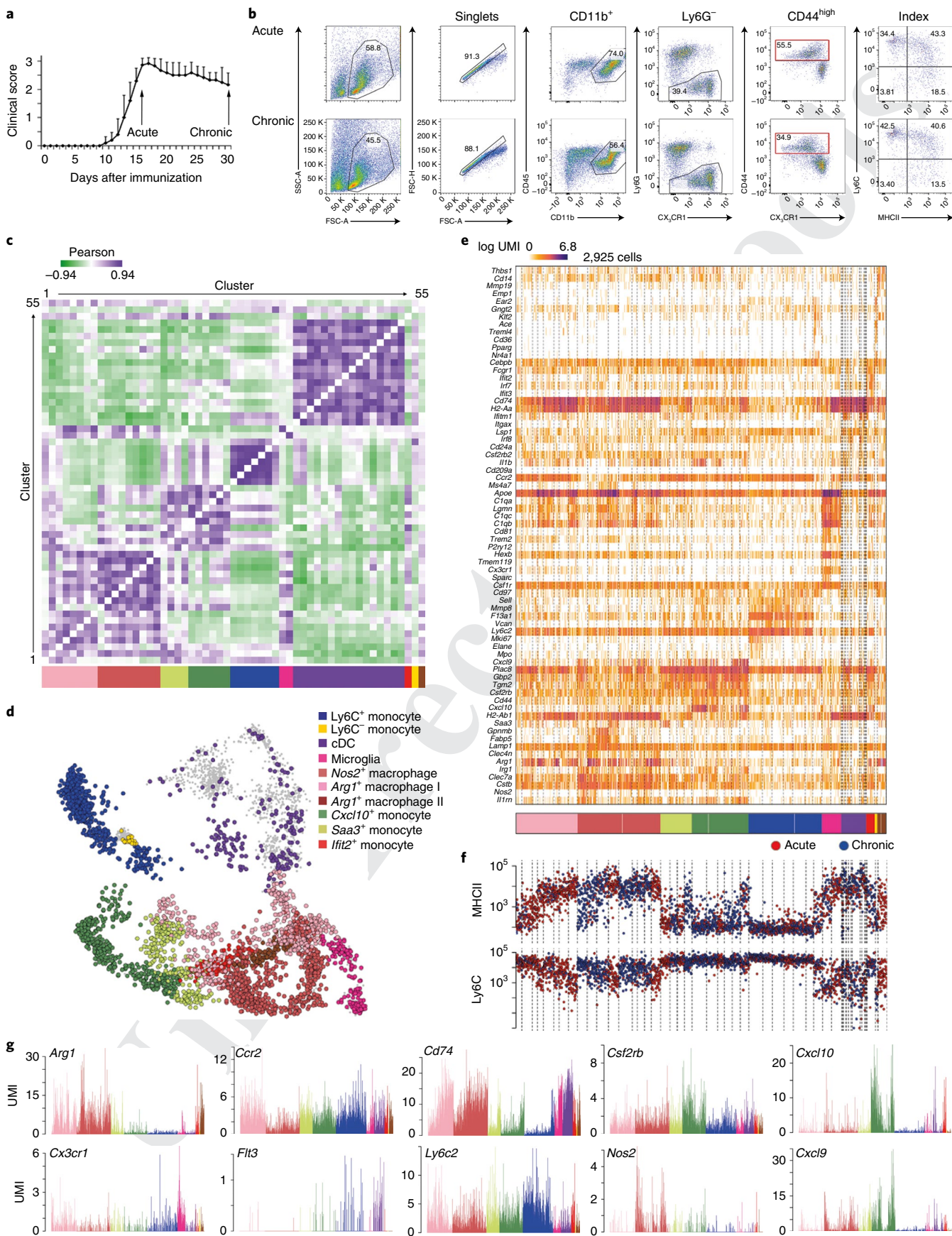
CNS-infiltrating monocytes do not express *Zbtb46* during EAE. At steady-state, *Zbtb46* is exclusively expressed in cDC^{20,21}, while monocyte-derived cells can induce expression of *Zbtb46* in vitro when cultured with CSF2 and interleukin 4 (IL-4)²². To test whether monocyte-derived cells acquired expression of *Zbtb46* during EAE, we immunized *Zbtb46*-GFP mice, which carry a green fluorescent protein (GFP) reporter under the control of the *Zbtb46* gene^{20,21}, with MOG₃₅₋₅₅ and analyzed mice at the peak of disease (day 15 PI, mean EAE score 2.7) and during the chronic phase (day 30 PI, mean EAE score 2.2; Extended Data Fig. 3a). We sorted at these two time points spinal cord-infiltrated CD11b⁺ cells, excluding Ly6G⁺ neutrophils and CX₃CR1^{hi}CD44^{lo} microglia, that express GFP (Extended Data Fig. 3b). Most *Zbtb46*-GFP⁺ cells (1,056 cells, 82%) could be assigned to the DC cluster (Extended Data Fig. 3c-e), indicating that expression of *Zbtb46* was largely restricted to the cDC lineage in vivo. These data suggested that the composition of cDCs, based on the transcriptome, was more uniform than that of macrophages and monocytes and most of the monocyte-derived cells such as *Arg1*⁺ and *Nos2*⁺ macrophages, *Saa3*⁺, *Cxcl10*⁺ and *Ifit2*⁺ monocytes do not induce expression of *Zbtb46* after tissue infiltration in EAE.

Acute and chronic EAE stages show distinct infiltration patterns. The composition of myeloid cells in the CNS during the course of EAE pathogenesis varies^{14,15}. To examine whether all ten myeloid cell clusters that we identified (Fig. 1d) emerged during the acute or chronic stages of disease, we examined the kinetics of each identified metacell cluster during these EAE stages (data for *Zbtb46*-GFP⁺ cell composition during acute and chronic stages can be found in the Extended Data Fig. 4). We detected a significant increase of *Cxcl10*⁺ monocytes during disease progression, from 8.8% in the acute phase to 21.2% in the chronic stage (Fig. 2b). We also found that the *Arg1*⁺ macrophage I subsets diminished during the course of disease, from 28.9% in the acute phase to 5.4% in the chronic phase, while *Nos2*⁺ macrophages increased during chronic disease stages (from 16.5% in acute to 27.8% in chronic stage, Fig. 2a,b). Correlation analysis

Fig. 1 | An atlas of mononuclear phagocytes in the inflamed CNS. **a**, Time-course of experimentally induced EAE in C57BL/6 mice after immunization with the MOG₃₅₋₅₅ peptide. Shown is the mean clinical score \pm s.e.m. $n=5$ mice for acute and $n=6$ for the chronic phase. **b**, Mean fluorescence intensity of Ly6C and MHCII on CD45⁺CD11b⁺Ly6G⁺CD44^{hi} cells. Red squares indicate sorted cells. **c**, Correlation analysis of the expression profiles of 2,925 infiltrated myeloid cells clustered into 55 distinct metacells according to their transcriptomic similarities. The size of the clusters in the correlation analysis is normalized and does not reflect the actual number of cells present in each cluster. Quality controls are shown in Extended Data Fig. 1 and pairwise analysis in Extended Data Fig. 2b. The color bar below indicates the ten main myeloid subsets based on correlation analysis. **d**, Two-dimensional projection of the metacell model of 2,925 isolated cells^{17,41}. Gray dots indicate additional *Zbtb46*⁺ cells introduced in Extended Data Fig. 3. **e**, Heatmap of the main signature genes per cluster in **d**. Full list of gene expression is presented in Supplementary Table 1. **f**, Index sorting tracks of recorded mean fluorescence intensity of Ly6C and MHCII protein expression of the cells in **e**. Red dots indicate cells isolated during the acute phase, while blue dots indicate cells from the chronic phase. **g**, Expression of genes in the cells in **e**. Cells are colored by their subset identity, as in **d**. Shown are UMIs per cell. For the experiments in **a-g**, we pooled $n=5$ animals for acute and $n=6$ for the chronic phase. The experiment was repeated twice with similar results.

130 already indicated that *Nos2*⁺ and the *Arg1*⁺ subsets were transcriptionally related (Fig. 1c and Extended Data Fig. 2b). We performed a
 131 differential gene expression analysis between *Nos2*⁺ and *Arg1*⁺ mac-
 132

rophages accordingly, which indicated that genes such as *Clec7a*,
 133 *Lgals3*, *Cxcl9* and *Cxcl16* were significantly upregulated in *Nos2*⁺
 134 cells compared to *Arg1*⁺ macrophages (Fig. 2c). *Arg1* itself is highly
 135



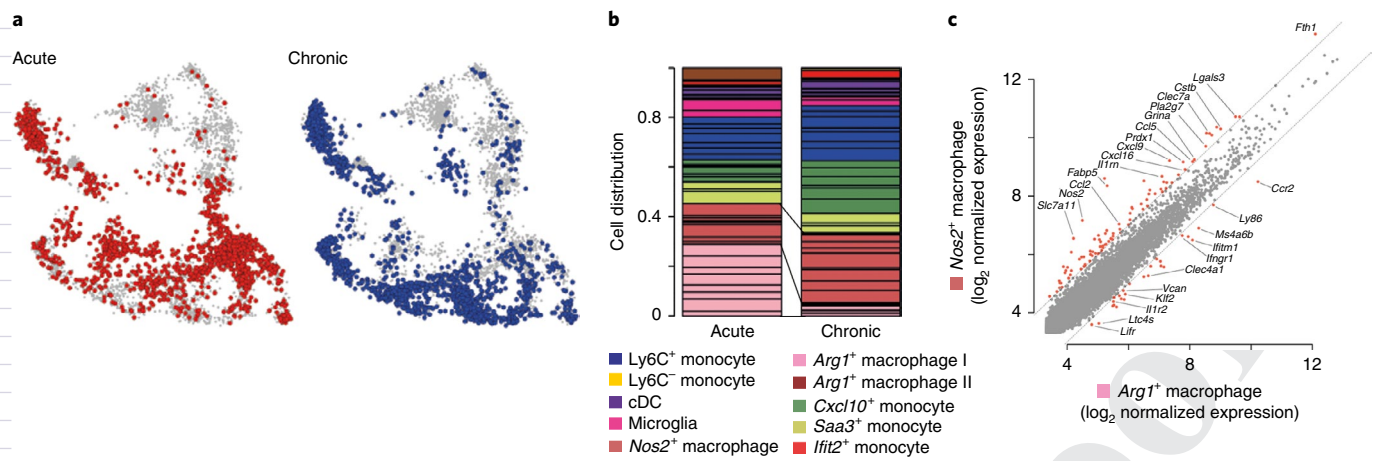


Fig. 2 | Temporal resolution of mononuclear phagocyte infiltrates in the acute and chronic stages of EAE. a, Projection of nonneutrophilic, nonmicroglial myeloid cells from Fig. 1 according to their time point of isolation. $n=1,373$ cells from acute (left) and 1,524 cells from chronic (right) EAE stages.

b, Cell distribution of mononuclear phagocytes at the acute and chronic stage of EAE. Cells are grouped by metacells and colored by the ten identified cell populations. Note the reduction of the $Arg1^+$ macrophage I subset at the chronic stage ($P < 10^{-50}$; false discovery rate, adjusted Fisher's exact test), while $Nos2$ -expressing cells increased during chronic disease stages ($P < 10^{-12}$, false discovery rate, adjusted Fisher's exact test). **c**, Differential gene expression between $Nos2^+$ macrophages and $Arg1^+$ macrophages I. Values represented \log -transformed normalized expression. For the experiments depicted in **a–c** we pooled $n=5$ animals for acute and $n=6$ for the chronic phase. The experiment was repeated twice with similar results.

expressed in both subsets and was not significant differentially expressed between $Nos2^+$ and $Arg1^+$ macrophages and therefore is not a specific marker for $Arg1^+$ macrophages.

Collectively, the close transcriptional relationship between $Arg1^+$ and $Nos2^+$ macrophages suggested that these subsets are interrelated and that $Nos2^+$ macrophages differentiate from $Arg1^+$ cells.

***Cxcl10*⁺ and *Saa3*⁺ monocytes are specifically depleted in the inflamed CNS after anti-CCR2 treatment.**

We next investigated whether the mononuclear phagocyte populations characterized by high expression of *Ccr2* (Fig. 1f) contributed to tissue damage during EAE pathogenesis. Antibody-mediated depletion of circulating CCR2⁺ immune cells by CCR2 antibody (MC21) injection reduces clinical symptoms in mice with EAE^{8,23}. To evaluate MC21 injection efficiency, we treated mice with EAE from day 16 PI with daily injections of 50 μ g MC21 or rat IgG2b antibodies for 6 consecutive days. When analyzed at day 21 PI, MC21-injected mice showed significant clinical improvement, evident by lower EAE scores, compared to mice treated with isotype antibodies (Extended Data Fig. 5a), indicating the efficiency of treatment with CCR2 antibody. However, to identify which CCR2⁺ monocyte subset carried potential pathogenic activity, we used a short-term treatment with MC21 to prevent additional, bystander effects potentially induced by long-term monocytes depletion. Therefore, we injected mice at the peak of disease (day 16 PI, mean EAE score, 3) with 50 μ g of MC21 (ref. ²⁴) or rat IgG2b antibodies once a day for 2 consecutive days. Flow cytometry analysis indicated the complete depletion of circulating Ly6C⁺ monocytes (Fig. 3a) and Ly6C⁺MHCII⁺ monocytes (Extended Data Fig. 5b) in the blood of MC21-treated, but not IgG2b-treated mice at day 18 PI, while Ly6C⁻ monocytes or other cells, such as splenic CD11c^{high}MHCII⁺ cDC1 or cDC2 subsets and FoxP3⁺ regulatory T cells (T_{reg} cells) were not affected (Fig. 3a and Extended Data Fig. 5c,d). We observed clinical improvements after the two MC21 injections compared to IgG2b-treated mice (Fig. 3b and Extended Data Fig. 5e). However, flow cytometry analysis using Ly6C and MHCII as surface markers, did not identify any changes in the frequency of Ly6C⁺MHCII⁻, Ly6C⁺MHCII⁺ and Ly6C⁻MHCII⁺ myeloid cell subsets (Fig. 3c). As such, we used scRNA-seq to profile specific myeloid subsets in the CNS of MC21- and IgG2b-treated mice at day 18 PI. Comparison of the most differentially expressed

genes in these two conditions indicated that inflammatory genes such as *Il1b*, *Cxcl10*, *Ifi47* and *Irf1* were strongly under-represented in the MC21-treated group (Fig. 3d), which could reflect their slightly improved health condition. To identify the origin of this pro-inflammatory signature, we isolated CD11b⁺Ly6G⁻CD44^{high} myeloid infiltrates from MC21- (433 cells) and isotype-treated (442 cells) mice and projected the single-cell transcriptomes onto our reference dataset (Fig. 1d and see Methods). We detected all myeloid subsets in isotype-treated mice including Ly6C⁺ and Ly6C⁻ monocytes, $Arg1^+$ and $Nos2^+$ macrophages, cDCs, microglia-like cells and $Saa3^+$ and $Cxcl10^+$ monocytes. When we compared the infiltration pattern of isotype-treated mice with MC21-treated mice, we observed that the $Saa3^+$ and $Cxcl10^+$ clusters were almost absent in the spinal cords of the MC21-treated mice (Fig. 3e,f). Similar results were obtained in an independent MC21-depletion experiment followed by scRNA-seq analysis, which was performed in a different mouse facility (Extended Data Fig. 5e–g). In summary, CCR2 antibody-mediated cell depletion achieves long-term alleviation of EAE symptoms, and is characterized by short-term specific depletion of $Saa3^+$ and $Cxcl10^+$ monocyte subsets in two independent experiments. These results highlight $Cxcl10^+$ cells as a unique cell population involved in pathological processes in the CNS of EAE mice.

***Cxcl10*⁺ monocytes are involved in CNS tissue damage.** To test whether the loss of $Cxcl10^+$ and $Saa3^+$ monocytes caused the attenuation of clinical symptoms in the MC21-treated mice either through the induction of transcriptomic changes in other immune cells or, alternatively, by affecting the cellular composition of the cells infiltrating the CNS, we performed MARS-seq on 2039 CD45⁺Ly6G⁻nonneutrophilic leukocytes infiltrating the CNS in MC21- and IgG2b-treated mice. Metacell analysis followed by annotation according to marker gene expression identified naive CD4⁺ T cells (characterized by the expression of *Thy1* and *Cd4*, but absence of *S100a4*), activated CD4⁺ T cells (*Cd4*, *Thy1* and *S100a4* expression), CD8⁺ T cells (*Cd8a* and *Nkg7* expression), T_{reg} cells (*Folr4* and *Tnfrsf4* expression), natural killer (NK) cells (*Il2rb* and *Gzma* expression), a minor fraction of B lymphocytes (*Cd74* and *Cd79b* expression), cDC (*Id2* and *Cd74* expression), monocytic cells (*Lyz2* and *Ccr2* expression) and microglia (*Hexb* and *ApoE* expression; Fig. 4a). We then compared the abundance of each annotated cell

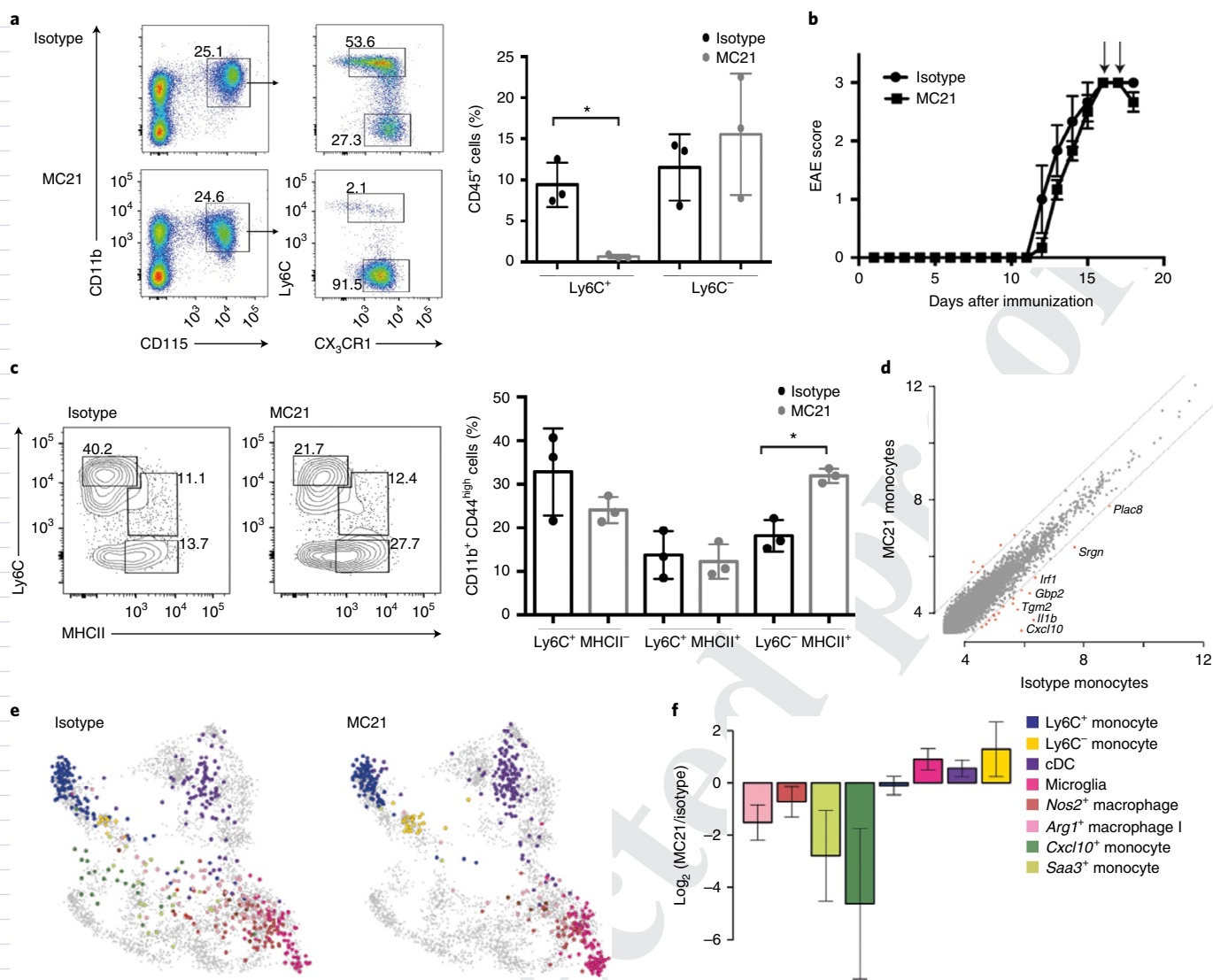


Fig. 3 | CCR2-mediated cell depletion uncovers pathogenic monocytes in the inflamed CNS. **a**, Representative fluorescence-activated cell sorting (FACS) plots of peripheral blood CD11b⁺CD115⁺Ly6C⁺ monocytes from mice treated with MC21 or isotype antibodies (left). Quantification of Ly6C⁻ and Ly6C⁺ monocyte populations in blood from MC21- or isotype-treated MOG-immunized C57BL/6 mice (right). Data are representative of three independent experiments with three mice. Asterisks indicate statistical significance of $P < 0.05$ from an unpaired two-tailed t -test. **b**, Time-course of EAE scores in MOG-immunized C57BL/6 mice treated with MC21 or isotype antibodies (day 16 PI, mean score in each group: 3 ± 0 s.e.m.; $n = 3$ mice). Shown is the mean clinical score \pm s.e.m. Arrows indicate antibody injections. **c**, Representative FACS plots of the distribution of Ly6C⁺MHC-II⁻, Ly6C⁺MHC-II⁺ and Ly6C⁻MHC-II⁺ subsets of myeloid infiltrates in the spinal cords of mice in **b** (left). Right, quantification of myeloid infiltrate subsets (right); mean \pm s.d. is shown, $n = 3$ mice; $P < 0.05$; unpaired two-tailed t -test. **d**, Differential gene expression analysis between pooled spinal cord infiltrating CD45⁺CD11b⁺Ly6G⁺CD44^{hi} myeloid single cells from MC21- and isotype-treated MOG⁻ immunized C57BL/6 mice, profiled by MARS-seq. **e**, Projection of CD45⁺CD11b⁺Ly6G⁺CD44^{hi} single cells isolated from spinal cords of isotype- (left) and MC21-treated (right) MOG⁻ immunized C57BL/6 mice on the metacell model from Fig. 1. **f**, Enrichment of myeloid subsets: Ly6C⁺ monocytes, Ly6C⁻ monocytes, cDCs, Microglia, Nos2⁺ macrophages, Arg1⁺ macrophages, Cxcl10⁺ monocytes and Saa3⁺ monocytes, in single cells from MC21-treated over isotype injected mice as in **e**. Values represent log₂ fold change over pooled data. Error bars represent 95% confidence intervals. **d-f**, Single cells from pooled spinal cords from $n = 3$ mice per group; $n = 442$ cells from isotype and 433 cells from MC21-treated animals were analyzed. A second and independent cell depletion MARS-seq experiment with purified MC21 is shown in Extended Data Fig. 5e-g.

type in MC21- and isotype-treated mice. We detected the absence of a monocyte cluster in mice that received two injections of MC21 antibody, while CD4⁺, CD8⁺, B and NK lymphocytes were equally present in MC21- and isotype-treated mice (Fig. 4b). Next, we performed differential gene expression analysis, comparing gene expression in different immune populations (naïve and activated CD4⁺ cells, CD8⁺ lymphocytes, microglia, cDC and monocytes) between MC21- and isotype-treated mice, to identify molecular changes that may arise from monocyte depletion. We were not able

to detect any gene changes in naïve and activated CD4⁺ cells, CD8⁺ lymphocytes, microglia and cDC irrespective of the presence or absence of Saa3⁺ and Cxcl10⁺ monocytes within the CNS (Fig. 4c). These data suggested the absence of Saa3⁺ and Cxcl10⁺ monocytes in the spinal cord, facilitated by CCR2 antibody-mediated cell depletion, did not lead to major gene changes in other immune cells, such as lymphocytes or microglia.

Next, we developed a flow cytometry-based approach to identify the Cxcl10⁺ and Arg1⁺ monocyte subsets ex vivo. Because CXCL10

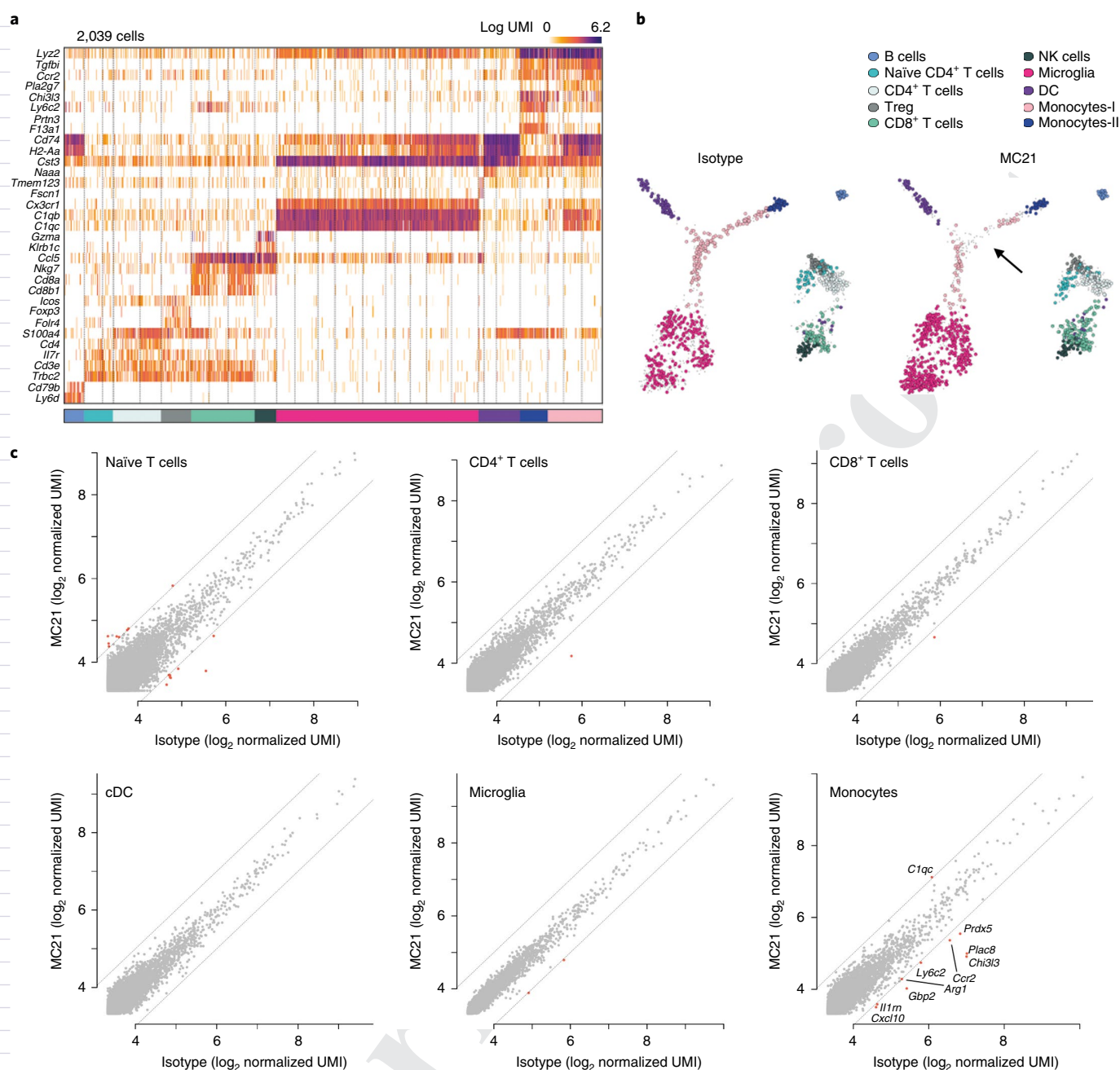


Fig. 4 | Monocyte depletion displays minor changes to other CNS-infiltrating cells. **a**, Gene expression profiles of 2059 CD45⁺Ly6G⁻ cells isolated from the spinal cord of isotype- and MC21-treated MOG-immunized C57BL/6 mice, clustered into 27 metacells that were grouped into ten cell states. **b**, Two-dimensional representation of all infiltrating CD45⁺Ly6G⁻ spinal cord cells in MOG-immunized C57BL/6 mice treated with isotype (left) or MC21 (right) antibodies. The different cell subsets are shown by color code. The arrow indicates the absence of monocyte II cells, corresponding to *Saa3*⁺ and *Cxcl10*⁺ cells, in the MC21-treated mice. **c**, Differential expression analysis within the main identified cell clusters. Shown are scatter blots of normalized UMI counts (in log₂) between isotype control and MC21-treated animals. B and NK cells were excluded from analysis due to low cell numbers. *n* = 3 animals per group were pooled for the experiments shown in **a–c**, and 972 cells from isotype and 1,087 cells from MC21-treated mice were sequenced.

385 antibodies suitable for flow cytometry are not commercially available and because *Cxcl10*⁺ monocytes coexpressed *Cxcl9* (Fig. 1g and Extended Data Fig. 2d), we tested whether antibodies against CXCL9 could be used alternatively to identify the *Cxcl10*⁺ monocyte subset. Based on the expression of *Cxcl9* and *Arg1* (and its protein product Arginase), we investigated whether staining for CXCL9 and Arginase would discriminate *Cxcl10*⁺ monocytes from *Nos2*⁺ macrophages (Extended Data Fig. 6). In the CNS of EAE mice at the peak of disease (day 17 PI), we detected CD45^{hi}Lin⁻CD11b⁺Ly6C⁺

cells that expressed either CXCL9 or Arginase (Fig. 5a). CXCL9⁺ cells had higher expression of Ly6C compared to Arginase⁺ cells (Fig. 5b). The specificity of the staining was confirmed by isotype control staining (Fig. 5c). Next, we isolated the CNS cell infiltrates of mice that were injected with MC21 or isotype antibody around peak of EAE (day 15 PI) for 2 d. CXCL9⁺Ly6C⁺ monocytes were virtually absent in MC21-treated mice compared to isotype-treated mice, while *Arginase*⁺ cells showed only a reduction tendency in MC21-treated mice compared to controls (Fig. 5e). To investigate whether

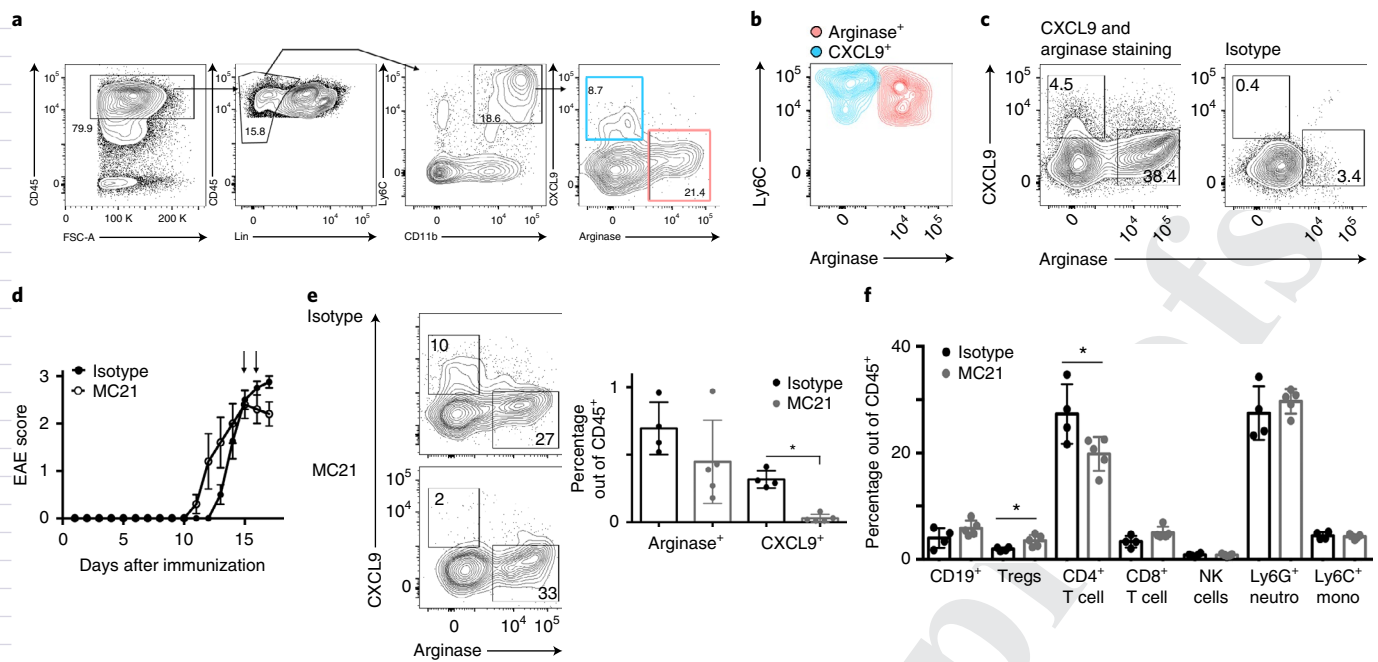


Fig. 5 | CXCL9 defines pathogenic infiltrating monocytes. **a, b**, Representative flow cytometry analysis of CD45^{hi}Lin⁻CD11b⁺Ly6C⁺ myeloid spinal cords infiltrates in MOG-immunized C57BL/6 at peak of disease (day 17 PI). Colored gates and populations indicate CXCL9⁺ (blue) and Arginase⁺ (encoded by *Arg1*, red) subsets. Data are representative of two independent experiments with three mice. **c**, Representative FACS plots of the samples from **a** stained for CXCL9 and Arginase, or for their isotype antibodies. Isotype control staining was performed twice. **d**, Time-course of EAE scores in MOG-immunized C57BL/6 mice treated with MC21 or isotype antibodies. (day 16 PI, mean score in each group: 3 ± 0 s.e.m.; $n = 3$ mice). Shown is the mean clinical score \pm s.e.m.. Arrows indicate time of antibody injections. **e**, Representative FACS plots of CXCL9⁺ and Arginase⁺ cells in the the Ly6C⁺ monocyte compartment in MOG-immunized C57BL/6 mice injected with MC21 or isotype antibodies as in **d** (left). Quantification of the CXCL9⁺ and Arginase⁺ fractions out of CD45⁺ cells (right). Mean \pm s.d.; * $P < 0.05$; unpaired two-tailed *t*-test. **f**, Quantification of immune subsets: CD19⁺ B cells, T_{regs}, CD4⁺ T cells, CD8⁺ T cells, NK cells, Ly6G⁺ neutrophils and Ly6C⁺ monocytes in the CNS of MOG-immunized C57BL/6 mice treated as in **d**, determined by flow cytometry. Shown are the frequencies (mean \pm s.d.) of the indicated cell populations out of CD45⁺ cells. T_{regs} were identified as CD4⁺FoxP3⁺. **d-f**, $n = 4$ (isotype) and $n = 5$ (MC21) mice per group; the experiment was repeated twice with similar results. * $P < 0.05$; unpaired two-tailed *t*-test.

the absence of CXCL9⁺Ly6C⁺ monocytes had an effect on the cellular composition in the CNS, we quantified the frequencies of lymphocytes and neutrophils in MC21- and isotype-treated mice. We detected a slight increase of CNS-infiltrated CD4⁺FoxP3⁺ T_{reg} cells from about 1.9% in IgG2b to 3.5% in MC21-treated mice, accompanied by a mild reduction of CD4⁺ T cells from about 27% in isotype-treated mice to 19.8% in MC21-treated mice (Fig. 5f). We did not observe significant changes to neutrophil levels between MC21- and isotype-treated mice. Together, these results showed that the depletion of *Cxcl10*⁺Ly6C⁺ monocytes did not induce a change in the gene expression of the immune cells in the CNS, and only slightly affected their composition, suggesting the *Cxcl10*⁺Ly6C⁺ monocytes might be directly involved in tissue damage.

Peripheral monocytes give rise to distinct myeloid subsets in the inflamed CNS. Emerging evidence suggests that the Ly6C⁺ monocyte compartment could be heterogeneous⁴⁵. To investigate the cellular origin of the different myeloid cells in the inflamed CNS, we injected 2×10^4 MDPs isolated from the bone marrow of CD45.1 wild-type mice into MOG-immunized CD45.2 wild-type mice shortly before the peak of disease (day 13 PI). Then, 48 h later, recipient mice received a second graft of 2×10^6 GFP⁺Ly6C⁺ monocytes isolated from the bone marrow of CD45.2 Ubc-GFP mice, which express GFP in all hematopoietic cells (Fig. 6a). Two days after the second injection, transferred CD45.2⁺GFP⁺ and CD45.1⁺ cells that also showed surface marker expression of Ly6C and MHCII, could be detected in the CNS of recipient mice (Fig. 6b). The transferred CD45.2⁺GFP⁺ and CD45.1⁺ cells were isolated from CNS at this

time point and analyzed by MARS-seq (Extended Data Fig. 7a-c). Consistent with MDPs being monocytes and cDC precursors²⁵, CD45.1⁺ MDP-derived cells included all myeloid lineages, including *Arg1*⁺ and *Nos2*⁺ macrophages, *Saa3*⁺ and *Cxcl10*⁺ monocytes and cDC (Fig. 6c). On the other hand, transferred GFP⁺Ly6C⁺ monocytes mainly gave rise to *Arg1*⁺ and *Nos2*⁺ cells, but not cDC or *Cxcl10*⁺ cells (Fig. 6c). Even when we analyzed recipient mice 4 d after the transfer of bone marrow Ly6C⁺ monocytes, we could not detect *Saa3*⁺ and *Cxcl10*⁺ cells derived from Ly6C⁺ monocytes (Extended Data Fig. 7d-f), suggesting that GFP⁺Ly6C⁺ monocytes lacked potential to differentiate into *Cxcl10*⁺ monocytes. CD45.2⁺ MDPs, as well as the GFP⁺Ly6C⁺ monocytes, also differentiated into cells with an activated microglia-like phenotype (Fig. 6c), as indicated by the high expression *Hexb*, *Sparc*, *C1qa*, *Cx3cr1* and *ApoE*, but lacking the expression of core microglia genes such as *P2ry12* and the transcription factor *Sall1* (ref. ²⁶), in line with a recent report²⁷.

To test whether monocytes needed peripheral education to develop into *Cxcl10*⁺ monocytes, we isolated splenic Ly6C⁺ monocytes from Ubc-GFP mice 6 d after MOG immunization and transferred 1×10^6 splenic GFP⁺Ly6C⁺ monocytes in mice with EAE at the peak of disease (day 14 PI) (Fig. 6d). Engrafted spleen-derived GFP⁺Ly6C⁺ cells could be detected in the CNS 2 d after transfer, but expressed less surface Ly6C than engrafted bone marrow-derived GFP⁺Ly6C⁺ monocytes (Fig. 6b,e). MARS-seq of the transferred spleen-derived GFP⁺Ly6C⁺ monocytes revealed that these cells efficiently differentiated into *Arg1*⁺, *Nos2*⁺ and microglia-like cells, but they did not give rise to *Saa3*⁺ or *Cxcl10*⁺ subsets 2 d after transfer (Fig. 6f).

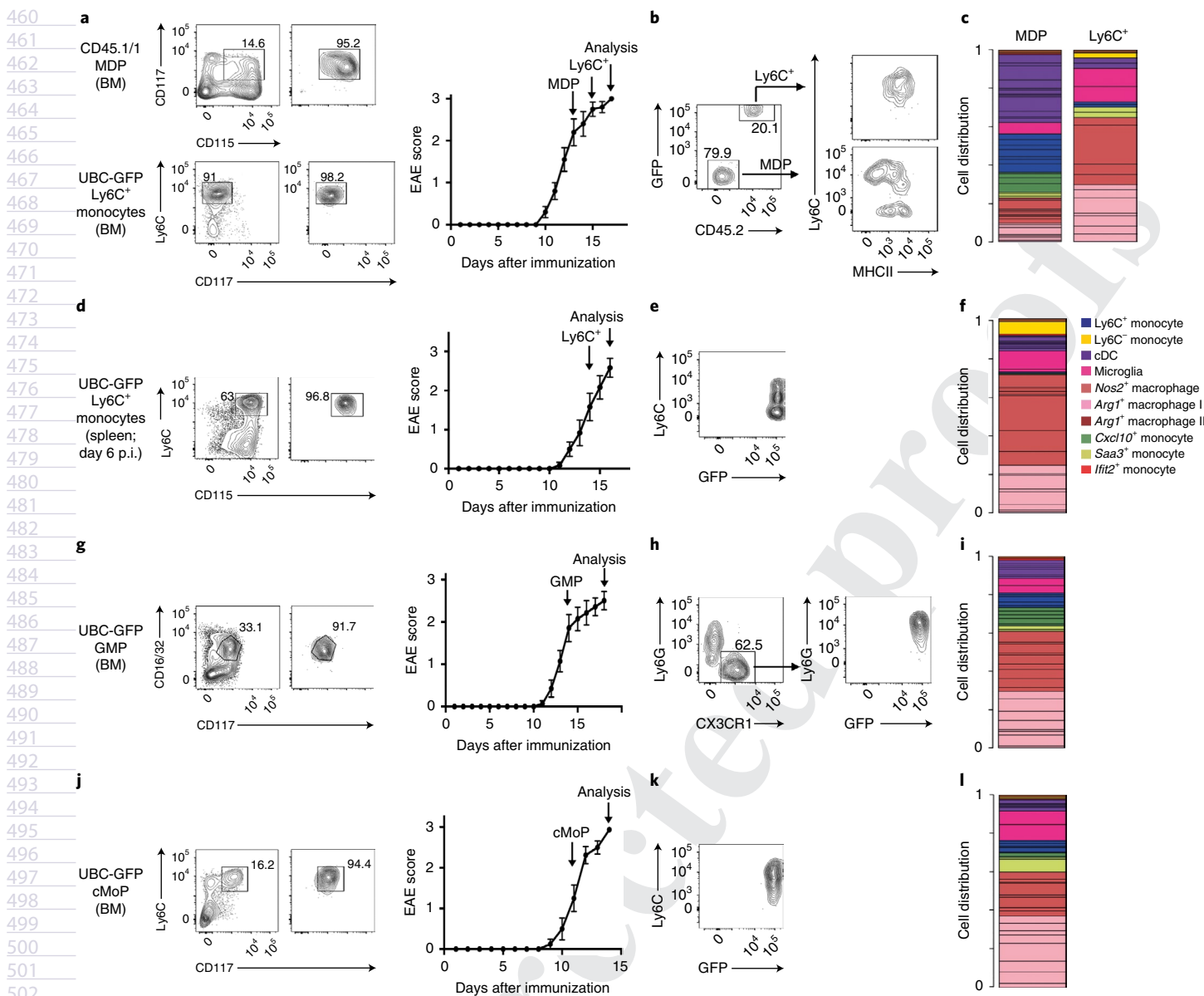


Fig. 6 | MDPs are the main precursors of CNS pathogenic monocytes. **a**, Scheme of the isolation of bone marrow-derived MDPs from CD45.1/1 mice, and bone marrow-derived Ly6C⁺ monocytes from UBC-GFP CD45.2/2 mice for transfer experiment (left). Time-course of EAE scores in MOG-immunized CD45.2/2 mice. Arrows indicate transfer of MDPs, transfer of bone-marrow (BM) monocytes, and time of analysis (right). Mean clinical score \pm s.e.m. is shown. **b**, Flow cytometry analysis of donor cells derived from CNS of MOG-immunized CD45.2/2 mice as in **a**. GFP and CD45.2 levels were used to separate MDP and bone-marrow-monocyte grafts. **c**, Myeloid subset distribution of 319 donor single cells profiled by MARS-seq and projected onto the metacell model from Fig. 1 based on their gene expression profiles. Index sorting measurements of CD45.2 and GFP were used to assign cells to either MDP or bone-marrow-monocyte graft origin (Extended Data Fig. 7a,b). Experiments shown in **a-c** were performed with *n*=10 EAE recipients. **d**, Scheme of the isolation of splenic Ly6C⁺ monocytes from MOG-immunized UBC-GFP CD45.2/2 mice (day 6 PI, *n*=6 mice) for transfer experiment (left). Time-course of EAE scores in MOG-immunized CD45.2/2 mice. Arrows indicate transfer of splenic monocytes, and time of analysis (right). Mean clinical score \pm s.e.m. is shown. **e**, Flow cytometry analysis of donor cells derived from CNS of CD45.2/2 mice as in **d**. **f**, Myeloid subset distribution of donor single cells profiled by MARS-seq and projected onto the metacell model from Fig. 1 based on their gene expression profiles. **d-f**, Six EAE recipients were used. **g**, Scheme of the isolation of bone marrow-derived GMPs from UBC-GFP CD45.2/2 for transfer experiment (left). Time-course of EAE scores in MOG-immunized CD45.2/2 mice (right). Arrows indicate transfer of GMPs, and time of analysis. Mean clinical score \pm s.e.m. is shown. **h**, Flow cytometry analysis of donor cells derived from CNS of CD45.2/2 mice as in **g**. **i**, Myeloid subset distribution of 105 Cx₃CR1⁺ donor GMP-derived single cells profiled by MARS-seq and projected onto the metacell model from Fig. 1 based on their gene expression profiles. **g-i**, Seven EAE recipients were used. **j**, Scheme of the isolation of bone marrow-derived cMoPs from UBC-GFP CD45.2/2 for transfer experiment (left). Time-course of EAE scores in MOG-immunized CD45.2/2 mice (right). Arrows indicate transfer of cMoPs, and time of analysis. Mean clinical score \pm s.e.m. is shown. **k**, Flow cytometry analysis of donor cells derived from CNS of CD45.2/2 mice as in **j**. **l**, Myeloid subset distribution of donor cMoP-derived single cells profiled by MARS-seq and projected onto the metacell model from Fig. 1 based on their gene expression profiles. **j-l**, Eight EAE recipients were used. Data in **a-l** are representative of one experiment.

526 Because GMPs were reported to give rise to monocytes *in vivo*⁷,
 527 we further tested the capacity of GMPs to differentiate into mono-
 528 cyte subsets under inflammatory conditions. We transferred 2×10^4
 529 Ubc-GFP⁺ GMPs in mice with EAE shortly before disease peak
 530 (day 14 PI) and analyzed the transferred cells in the CNS 4 d later
 531 (Fig. 6g). GFP⁺ GMPs gave rise to Ly6G⁺ neutrophils as expected⁷,
 532 but also Ly6C⁺CX₃CR1⁺ cells could be found in the CNS (Fig. 6h).
 533 MARS-seq of the latter established that monocytic GMP descen-
 534 dants can develop into all subsets identified in the CNS, including
 535 Ly6C⁺ monocytes, microglia-like cells, *Arg1*⁺ and *Nos2*⁺ macro-
 536 phages, *Cxcl10*⁺ and *Saa3*⁺ and, albeit with a lower frequency than
 537 MDPs, into DCs (Fig. 6i). A similar differentiation potential was
 538 observed when 1×10^5 GFP⁺ cMoP were transferred into EAE mice
 539 at day 11 PI, 3 d before the peak of disease (Fig. 6j–l). Transferred
 540 GFP⁺ cMoP were able to give rise to microglia-like cells, *Arg1*⁺,
 541 *Nos2*⁺ and *Cxcl10*⁺ subsets. These data indicated that *Cxcl10*⁺ mono-
 542 cytes were derived from MDP, GMP and partially cMoP myeloid
 543 progenitors, while Ly6C⁺ monocytes developed less efficiently into
 544 the *Saa3*⁺ and *Cxcl10*⁺ monocytes.

545

546 Discussion

547 Here, we used MARS-seq in combination with index sorting to
 548 characterize the mononuclear phagocytes that infiltrated the spinal
 549 cord during acute and chronic stages of EAE pathogenesis. We iden-
 550 tified a total of eight monocyte subsets or activation stages and three
 551 defined DC clusters, of which a subset of *Cxcl10*⁺ monocytes were
 552 characterized by a pathogenic signature.

553 EAE is a T cell-initiated, monocyte-driven murine autoimmune
 554 disease^{11,28}. Initial histological attempts to investigate the myeloid
 555 cells in the demyelinating lesions in the CNS of MS patients has sug-
 556 gested the heterogeneity of monocytes and macrophages or microg-
 557 lia, which was affected by the localization within the lesion and by
 558 the disease stage^{29,30}. Histology studies in *iNos*-tdTomato/*Arg1*-YFP
 559 or *LysM*-eGFP/*CD11c*-eYFP reporter mice provided important
 560 insight into the spatial and temporal composition of macrophages
 561 in EAE^{14,15}. In the *iNos*-tdTomato/*Arg1*-YFP reporter mice, *iNos*-
 562 tdTomato⁺ *Arg1*-YFP⁻ cells sequentially developed into *iNos*-tdTo-
 563 mato⁻ *Arg1*-YFP⁺ cells, which was interpreted as a conversion of
 564 pro-inflammatory *iNos*⁺ cells into anti-inflammatory *Arg1*⁺ cells
 565 during EAE progression¹⁴. However, the data presented here sug-
 566 gest a more complex mononuclear phagocyte composition in the
 567 CNS, with more than one linear developmental potential from a
 568 pro-inflammatory to anti-inflammatory phenotype. We observed
 569 two related myeloid subsets characterized by expression of *Nos2* and
 570 *Arg1*, a hallmark of myeloid-derived suppressor cells³¹, and these
 571 two subsets seemed to undergo a transcriptomic switch during the
 572 course of disease. Notably, *Nos2*⁺ cells also expressed high amounts
 573 of *Arg1*, and the two populations were comparable at the transcrip-
 574 tional level, suggesting that these cells are related and develop into
 575 each other, corroborating the earlier report¹⁴.

576 However, even if the *Arg1*⁺ and *Nos2*⁺ macrophages were read-
 577 ily detectable during EAE progression and accounted for a large
 578 proportion of the myeloid cell infiltrate, they lacked a pro-inflam-
 579 matory signature. Instead, we identified the *Cxcl10*⁺ and *Saa3*⁺
 580 monocyte subsets as the main myeloid subsets with a pathogenic
 581 profile in the inflamed CNS. These cells were characterized by
 582 high expression of surface Ly6C, were depleted by an CCR2 anti-
 583 body and expressed *Csf2rb* and *Il1b*. The expression of CSF2 is a
 584 prerequisite for EAE development, because *Csf2*^{-/-} mice show a
 585 complete resistance toward EAE development³². It is known that
 586 CSF2 exerts its function by targeting CCR2⁺ cells¹¹. Of note, mono-
 587 cytes with genetically impaired signaling through the CSF2 are still
 588 able to infiltrate the spinal cord during EAE, but lack pathogenic
 589 activity³³. Collectively, these data demonstrate that CSF2 is not
 590 merely a survival factor, but rather plays a role in the functional
 591 education of monocytes.

Of note, peripheral *Cxcl10*⁺ cells were identified in the lymph nodes
 of mice infected intradermally with different pathogens, includ-
 ing the nematode *Nippostrongylus brasiliensis*, the fungi *Candida*
albicans and *Mycobacterium smegmatis*³⁴, and possibly in malaria³⁵.
 These results may indicate that *Cxcl10*⁺ monocytes are an
 emergency population that differentiates during various inflamma-
 tory conditions. It is important to know where these cells originate
 from. Two distinct CCR2-dependent Ly6C⁺ monocyte subsets,
 with distinct fates during inflammatory conditions, have been
 described: classical Ly6C⁺MHCII⁻*CD209a*⁻ monocytes and
 Ly6C⁺MHCII⁺*Cd209a*⁺ cells⁵. When mice were infected with
Listeria monocytogenes, Ly6C⁺MHCII⁻*Cd209a*⁻ monocytes differ-
 entiated into *iNos*⁺ cells, which were previously named TipDCs³⁶.
 Our data support this observation, because Ly6C⁺ monocytes
 gave rise preferentially to *Nos2*⁺ and *Arg1*⁺ cells in mice with EAE
 after transfer. Ly6C⁺MHCII⁺*Cd209a*⁺ cells on the other hand were
 dependent on CSF2 and CCR2 and had a DC phenotype during
Listeria infection⁵, but their exact function during pathogenesis
 remains unclear. However, further sensitive and specific fate map-
 ping systems are needed to clarify the origin and fate of pathogenic
 monocyte subsets in the future.

Another question arising from our study is, how do pathogenic
 monocytes contribute to tissue damage and disease progression?
Cxcl10⁺ cells had high expression of *Il1b*. IL-1 β secretion by CCR2⁺
 monocytes was shown to be important for their transmigration
 across the blood–brain barrier and the proper activation of autore-
 active CD4⁺ T cells^{37,38}. CXCL10 itself is also involved in the recruit-
 ment of activated CD4⁺ T cells via CXCR3, and neutralization of
 CXCL10 by antibody treatment leads to decreased clinical symp-
 toms in mice with EAE³⁹. Taken together, our analysis revealed the
 presence of a previously unknown monocyte subset with a unique
 phenotype in the spinal cord of mice with EAE. It seems that these
 cells exhibit direct pathogenic function with minimal influences on
 other immune cells. Because *Cxcl10*⁺ monocytes were also reported
 in other inflammatory conditions^{34,35} and probably also in cancer⁴⁰,
 specific targeting of these cells might represent a promising strategy
 for therapeutic intervention in MS and other pathologies.

Online content

Any methods, additional references, Nature Research reporting
 summaries, source data, extended data, supplementary informa-
 tion, acknowledgements, peer review information; details of author
 contributions and competing interests; and statements of data and
 code availability are available at <https://doi.org/10.1038/s41590-020-0661-1>.

Received: 28 May 2019; Accepted: 13 March 2020;

References

- Geissmann, F., Jung, S. & Littman, D. R. Blood monocytes consist of two principal subsets with distinct migratory properties. *Immunity* **19**, 71–82 (2003).
- Carlin, L. M. et al. Nr4a1-dependent Ly6C(low) monocytes monitor endothelial cells and orchestrate their disposal. *Cell* **153**, 362–375 (2013).
- Mildner, A., Yona, S. & Jung, S. A close encounter of the third kind: monocyte-derived cells. *Adv. Immunol.* **120**, 69–103 (2013).
- Mildner, A. et al. Genomic characterization of murine monocytes reveals *C/EBP β* transcription factor dependence of Ly6C⁻ cells. *Immunity* **46**, 849–862.e7 (2017).
- Menezes, S. et al. The heterogeneity of Ly6Chi monocytes controls their differentiation into *iNOS*⁺ macrophages or monocyte-derived dendritic cells. *Immunity* **45**, 1205–1218 (2016).
- Yáñez, A. et al. Granulocyte-monocyte progenitors and monocyte-dendritic cell progenitors independently produce functionally distinct monocytes. *Immunity* **47**, 890–902.e4 (2017).
- Liu, Z. et al. Fate mapping via Ms4a3-expression history traces monocyte-derived cells. *Cell* **178**, 1509–1525.e19 (2019).
- Mildner, A. et al. CCR2⁺Ly-6C^{hi} monocytes are crucial for the effector phase of autoimmunity in the central nervous system. *Brain* **132**, 2487–2500 (2009).

9. King, I. L., Dickendesher, T. L. & Segal, B. M. Circulating Ly-6C⁺ myeloid precursors migrate to the CNS and play a pathogenic role during autoimmune demyelinating disease. *Blood* **113**, 3190–3197 (2009).
10. Ajami, B., Bennett, J. L., Krieger, C., McNagny, K. M. & Rossi, F. M. V. Infiltrating monocytes trigger EAE progression, but do not contribute to the resident microglia pool. *Nat. Neurosci.* **14**, 1142–1149 (2011).
11. Croxford, A. L. et al. The cytokine GM-CSF drives the inflammatory signature of CCR2⁺ monocytes and licenses autoimmunity. *Immunity* **43**, 502–514 (2015).
12. Spath, S. et al. Dysregulation of the cytokine GM-CSF induces spontaneous phagocyte invasion and immunopathology in the central nervous system. *Immunity* **46**, 245–260 (2017).
13. Jaitin, D. A. et al. Massively parallel single-cell RNA-Seq for marker-free decomposition of tissues into cell types. *Science* **343**, 776–779 (2014).
14. Locatelli, G. et al. Mononuclear phagocytes locally specify and adapt their phenotype in a multiple sclerosis model. *Nat. Neuroscience* **21**, 1196–1208 (2018).
15. Caravagna, C. et al. Diversity of innate immune cell subsets across spatial and temporal scales in an EAE mouse model. *Sci. Rep.* **8**, 5146 (2018).
16. Lewis, N. D., Hill, J. D., Juchem, K. W., Stefanopoulos, D. E. & Modis, L. K. RNA sequencing of microglia and monocyte-derived macrophages from mice with experimental autoimmune encephalomyelitis illustrates a changing phenotype with disease course. *J. Neuroimmunol.* **277**, 26–38 (2014).
17. Giladi, A. et al. Single-cell characterization of haematopoietic progenitors and their trajectories in homeostasis and perturbed haematopoiesis. *Nat. Cell Biol.* **20**, 836–846 (2018).
18. Baran, Y. et al. MetaCell: analysis of single-cell RNA-seq data using K-nn graph partitions. *Genome Biol.* **20**, 206–219 (2019).
19. Butler, A., Hoffman, P., Smibert, P., Papalexi, E. & Satija, R. Integrating single-cell transcriptomic data across different conditions, technologies, and species. *Nat. Biotechnol.* **36**, 411–420 (2018).
20. Meredith, M. M. et al. Zinc finger transcription factor zDC is a negative regulator required to prevent activation of classical dendritic cells in the steady state. *J. Exp. Med.* **209**, 1583–1593 (2012).
21. Satpathy, A. T. et al. Zbtb46 expression distinguishes classical dendritic cells and their committed progenitors from other immune lineages. *J. Exp. Med.* **209**, 1135–1152 (2012).
22. Briseño, C. G. et al. Distinct transcriptional programs control cross-priming in classical and monocyte-derived dendritic cells. *Cell Rep.* **15**, 2462–2474 (2016).
23. Wolf, Y. et al. Microglial MHC class II is dispensable for experimental autoimmune encephalomyelitis and cuprizone-induced demyelination. *Eur. J. Immunol.* **48**, 1308–1318 (2018).
24. Brühl, H. et al. Targeting of Gr-1⁺, CCR2⁺ monocytes in collagen-induced arthritis. *Arthritis Rheum.* **56**, 2975–2985 (2007).
25. Varol, C. et al. Monocytes give rise to mucosal, but not splenic, conventional dendritic cells. *J. Exp. Med.* **204**, 171–180 (2007).
26. Matcovitch-Natan, O. et al. Microglia development follows a stepwise program to regulate brain homeostasis. *Science* **353**, aad8670–aad8670 (2016).
27. Shemer, A. et al. Engrafted parenchymal brain macrophages differ from microglia in transcriptome, chromatin landscape and response to challenge. *Nat. Commun.* **9**, 5206 (2018).
28. Becher, B., Tugues, S. & Greter, M. GM-CSF: from growth factor to central mediator of tissue inflammation. *Immunity* **45**, 963–973 (2016).
29. Esiri, M. M. & Reading, M. C. Macrophage populations associated with multiple sclerosis plaques. *Neuropathol. Appl. Neurobiol.* **13**, 451–465 (1987).
30. Brück, W. et al. Monocyte/macrophage differentiation in early multiple sclerosis lesions. *Ann. Neurol.* **38**, 788–796 (1995).
31. Melero-Jerez, C., Ortega, M. C., Moliné-Velázquez, V. & Clemente, D. Myeloid derived suppressor cells in inflammatory conditions of the central nervous system. *Biochim. Biophys. Acta.* **1862**, 368–380 (2016).
32. McQualter, J. L. et al. Granulocyte macrophage colony-stimulating factor: a new putative therapeutic target in multiple sclerosis. *J. Exp. Med.* **194**, 873–882 (2001).
33. Greter, M. et al. GM-CSF controls nonlymphoid tissue dendritic cell homeostasis but is dispensable for the differentiation of inflammatory dendritic cells. *Immunity* **36**, 1031–1046 (2012).
34. Blecher-Gonen, R. et al. Single-cell analysis of diverse pathogen responses defines a molecular roadmap for generating antigen-specific immunity. *Cell Syst.* **8**, 109–121.e6 (2019).
35. Hirako, I. C. et al. Splenic differentiation and emergence of CCR5⁺CXCL9⁺CXCL10⁺ monocyte-derived dendritic cells in the brain during cerebral malaria. *Nat. Commun.* **7**, 13277–19 (2016).
36. Serbina, N. V., Salazar-Mather, T. P., Biron, C. A., Kuziel, W. A. & Pamer, E. G. TNF/iNOS-producing dendritic cells mediate innate immune defense against bacterial infection. *Immunity* **19**, 59–70 (2003).
37. Paré, A. et al. IL-1 β enables CNS access to CCR2hi monocytes and the generation of pathogenic cells through GM-CSF released by CNS endothelial cells. *Proc. Natl Acad. Sci. USA* **115**, E1194–E1203 (2018).
38. Ronchi, F. et al. Experimental priming of encephalitogenic Th1/Th17 cells requires pertussis toxin-driven IL-1 β production by myeloid cells. *Nat. Commun.* **7**, 11541 (2016).
39. Fife, B. T. et al. CXCL10 (IFN-gamma-inducible protein-10) control of encephalitogenic CD4⁺ T cell accumulation in the central nervous system during experimental autoimmune encephalomyelitis. *J. Immunol.* **166**, 7617–7624 (2001).
40. Zilionis, R. et al. Single-cell transcriptomics of human and mouse lung cancers reveals conserved myeloid populations across individuals and species. *Immunity* **50**, 1317–1334 (2019).
41. Cohen, M. et al. Lung single-cell signaling interaction map reveals basophil role in macrophage imprinting. *Cell* **175**, 1031–1044.e18 (2018).

Publisher's note Springer Nature remains neutral with regard to jurisdictional claims in published maps and institutional affiliations.

© The Author(s), under exclusive licence to Springer Nature America, Inc. 2020

Methods

Mice. Mice were maintained in a special pathogen-free, temperature-controlled (22 ± 1 °C) mouse facility on a reverse 12-h light, 12-h dark cycle at the Max-Delbrück Center, Berlin, Germany, or the Weizmann Institute of Science, Rehovot, Israel. Food and water were given ad libitum. Mice were fed a usual chow diet.

The 8–12-week-old female C57BL/6 mice and Zbtb46^{Gfp/+} mice (B6.129S6(C)-Zbtb46^{tm1.1Kmm/J}) were immunized subcutaneously with 200 µg of MOG₃₅₋₅₅ peptide emulsified in complete Freund's adjuvant containing 1 mg of *Mycobacterium tuberculosis* (H37RA, Difco Laboratories) as described previously⁸. Mice received intraperitoneal injections of 250 ng pertussis toxin (Sigma-Aldrich) at the time of immunization and 48 h later. Mice were scored daily as follows: 0, no detectable signs of EAE; 0.5, distal limp tail; 1.0, complete limp tail; 1.5, limp tail and hind limb weakness; 2, unilateral partial hind limb paralysis; 2.5, bilateral partial hind limb paralysis; 3, complete bilateral hind limb paralysis and 3.5, complete hind limb paralysis and unilateral forelimb paralysis.

For adoptive transfer experiments, EAE-diseased mice received an intravenous injection of 2 × 10⁴ MDPs (Lin^{neg} (TCRγδ, NK1.1, TCRβ, B220), CD135⁺, CD115⁺, CD117⁺, CD11b⁻) from female CD45.1/1 mice (B6.SJL-PtprcaPep3b/BoyJ) shortly before the peak of disease. Then, 48 h later, the same mice received an injection of 2 × 10⁶ Ly6C⁺ GFP⁺ bone marrow monocytes (Lin^{neg}, CD135⁺, CD117⁺, MHCII⁻, CD11b⁺, CD115⁺, Ly6C⁺ from female Ubiquitin-GFP mice; C57BL/6-Tg(UBC-GFP)30Scha/J) and CNS cells were isolated 48 h after the last injection. GMPs (Lin^{neg}, CD135⁻, CD117⁺, CD34⁺, CD16/32⁺, CD11b⁻, CD115⁻, Ly6C⁻) were identified according to ref. ⁷, and 2 × 10⁶ GMP were transferred 4 d before the peak of disease. Then 1 × 10⁵ cMoPs (Lin^{neg}, CD135⁻, CD117⁺, CD11b⁻, CD115⁺, Ly6C⁺) were isolated as reported in ref. ⁴². For cell depletion experiments, 50 µg of purified antibodies (or 100 µl MC21 hybridoma as indicated) were injected at the peak of disease for 2 consecutive days. Mice were analyzed 1 d after the last injection. Rat IgG2b served as control antibody in all experiments. All animal experiments have been approved by the LAGEso in Berlin or by the Weizmann Institute Animal Care Committee in accordance with international guidelines.

Flow cytometry. For peripheral blood analysis, blood was collected and mononuclear cells were enriched by Ficoll density gradient centrifugation (2,200 r.p.m., 15 min at 20 °C with low acceleration and no brake). For CNS analysis mice were perfused with 5 ml PBS via the left ventricle and spinal cord samples were harvested from individual mice. CNS tissues were cut into small pieces and homogenized through a 100-µm mesh filter without tissue digestion. After washing, the cell pellet was resuspended in 40% Percoll and the myelin fraction was separated from mononuclear cells by density centrifugation (2,200 r.p.m., 20 min at 14 °C with low acceleration and no brake). MDPs from the bone marrow were MACS pre-enriched by antiCD135 biotin antibody followed by antibiotin microbeads (Miltenyi). GMPs were pre-enriched with antiCD117 microbeads (Miltenyi). Bone marrow and splenic Ly6C⁺ monocytes and cMoPs were pre-enriched by antiCD115 biotin antibody followed by antibiotin microbeads (Miltenyi). All cells, except for GMP isolation, were blocked before staining with antiCD16/32 (93) and antibodies against B220 (RA3-6B2), CD11b (M1/70), CD11c (N418), CD115 (AFS98), CD117 (2B8), Ly6C (HK1.4), CD135 (A2F10), Ly6G (1A8), CD19 (6D5), CD3e (145-2c11), CD4 (GK1.5), CD45 (30-F11), CD45.1 (A20), CD45.2 (1D4), CD8a (53-6.7), NK1.1 (PK136), I-A^b (MHCII; AF6-120.1), CX3CR1 (SA011F11), CD16/32 (93), CD34 (SA376A4), FoxP3 (FJK-16s), CXCL9 (MIG-2F5.5), Arginase (A1exF5) and CD44 (IM7) from Biologend or eBioscience were used. For CXCL9 and Arginase stainings, Percoll-isolated mononuclear infiltrates were incubated in full RPMI media supplemented with 1 × Brefeldin A at 37 °C for 3 h. Intracellular stainings were performed with the Biologend FoxP3 fix/perm kit. Samples were flow sorted using AriaII, AriaIII or Aria-Fusion (BD Biosciences, BD Diva Software) cell sorter. Antalysis was performed on Fortessa or LSRII (BD Biosciences, BD Diva Software) and analyzed with FlowJo software v.10.5.3 (Treestar).

scRNA-sequencing. Single-cell libraries were prepared with MARS-seq method¹³. In brief, messenger RNA from single cells sorted into cell capture plates was barcoded and converted into complementary DNA and pooled using an automated pipeline. Subsequently, the pooled sample was linearly amplified by T7 in vitro transcription, and resulting RNA was fragmented and converted into a sequencing-ready library by tagging the samples with pool barcodes and Illumina sequences during ligation, reverse transcription and PCR. Each pool of cells was tested for library quality and library concentration was assessed. scRNA-seq libraries (pooled at equimolar concentration) were sequenced on an Illumina NextSeq 500 at a median sequencing depth of 52,030 reads per cell.

Single-cell analysis. For low-level processing and filtering, sequences were mapped to mouse genome (mm9), demultiplexed and filtered as previously described¹³, extracting a set of unique molecular identifiers (UMIs) that define distinct transcripts in single cells for further processing. Mapping of reads was done using HISAT (v.0.1.6)⁴³; reads with multiple mapping positions were excluded. Reads were associated with genes if they were mapped to an exon, using the UCSC genome browser for reference. Cells with fewer than 500 UMIs were discarded from the analysis. After filtering, cells contained a median of 2,269 unique molecules per cell. All downstream analysis was performed in R.

The metacell pipeline¹⁸ was used to derive informative genes and compute cell-to-cell similarity, to compute K-nn graph covers and derive distribution of RNA in cohesive groups of cells (or metacells), and to derive strongly separated clusters using bootstrap analysis and computation of graph covers on resampled data. Default parameters were used unless otherwise stated. For Figs. 1 and 2, a metacell cover was produced on a combined dataset of myeloid and Zbtb46-GFP⁺ cells from acute and chronic stages of the disease.

Two-dimensional visualization of the metacell structure was performed as previously described^{17,18}. In short, a symmetric graph is constructed over all metacells, by thresholding over the coclustering statistics (indicating how cells from two distinct metacells are likely to be clustered together). This results in a graph with maximum degree, *D*, and any number of connected components. MetaCell computes coordinates for each metacell by applying a standard force-directed layout algorithm to the graph. It then positions cells by averaging the metacell coordinates of their neighbor cells in the K-nn graph, but filter neighbors that define a metacell pair that is not connected in the graph.

MetaCell approximates the gene expression intensity within each metacell by a regularized geometric mean. It then quantifies relative expression as the log-fold enrichment over the median metacell value (lfp, a complete list of lfp gene expression is shown in Supplementary Table 1). To annotate metacells and assign them into monocyte and macrophage states, we implemented a supervised approach, where metacells are assigned (or colored) into functional groups by expression of a curated list of marker genes. Each marker is assigned a threshold value, and all metacells whose lfp value for that marker are above the threshold are colored for that marker. In case of a conflict, a priority parameter can help decide which marker trumps assignment by other markers.

To project a new set of single-cell profiles on the existing reference metacell model from Fig. 1 (Figs. 3 and 6 and Extended Data Fig. 5), we extract for each new cell the ten reference cells with top Pearson correlation over the normalized gene features defined for the reference model. The distribution of cluster memberships over these K-neighbors is used to associate the new cell with a reference metacell (by majority voting) and to project the cell in two dimensions by weighted average of the linked reference clusters' mapped *x* and *y* coordinates.

Pathway enrichment analysis was performed with clusterProfiler v.3.8.1 (ref. ⁴⁴), using a Benjamini–Hochberg-adjusted *P* ≤ 0.05 as the significance threshold. REVIGO was used to refine enriched groups and remove redundant terms⁴⁵.

Reporting Summary. Further information on research design is available in the Nature Research Reporting Summary linked to this article.

Data availability

Data generated during this study have been deposited in Gene Expression Omnibus⁴⁶ with the accession code GSE144317.

Code availability

Scripts and auxiliary data needed to reconstruct analysis files will be made available by request.

References

- Hettinger, J. et al. Origin of monocytes and macrophages in a committed progenitor. *Nat. Immunol.* **14**, 821–830 (2013).
- Kim, D., Langmead, B. & Salzberg, S. L. HISAT: a fast spliced aligner with low memory requirements. *Nat. Methods.* **12**, 357–360 (2015).
- Yu, G., Wang, L.-G., Han, Y. & He, Q.-Y. clusterProfiler: an R package for comparing biological themes among gene clusters. *OMICS* **16**, 284–287 (2012).
- Supek, F., Bošnjak, M., Škunca, N. & Šmuc, T. REVIGO summarizes and visualizes long lists of gene ontology terms. *PLoS ONE* **6**, e21800 (2011).

Acknowledgements

We thank V. Malchin for excellent technical support, J. Priller for support, the MDC animal facility (especially J. Bergemann) and the MDC and WIS FACS facilities (especially H.-P. Rahn). A.M. is a Heisenberg fellow supported by the DFG (MI1328). I.A. is supported by the Chan-Zuckerberg Initiative, the HHMI International Scholar award, the European Research Council Consolidator grant (no. ERC-COG) 724471-HemTree2.0, the Thompson Family Foundation, an MRA Established Investigator Award (509044), the Israel Science Foundation (703/15), the Ernest and Bonnie Beutler Research Program for Excellence in Genomic Medicine, the Helen and Martin Kimmel award for innovative investigation, an International Progressive MS Alliance/NMSS PA-1604-08459 and an Adelis Foundation grant. S.J. is supported by the International Progressive MS Alliance/NMSS PA-1604-08459.

Author contributions

A.M. designed and, together with I.A., supervised the study. L.K.W., H.L., D.D., C.M., F.P. and A.S. performed the experiments. A.G. performed bioinformatical analysis. S.J., S.Y., M.M. and A.L. provided key reagents/mouse lines and intellectual input. A.M. and I.A. wrote the manuscript.

Competing interests

The authors declare no competing interests.

724 **Additional information**
725 **Extended data** is available for this paper at <https://doi.org/10.1038/s41590-020-0661-1>.
726 **Supplementary information** is available for this paper at <https://doi.org/10.1038/s41590-020-0661-1>.
727
728
729
730
731
732
733
734
735
736
737
738
739
740
741
742
743
744
745
746
747
748
749
750
751
752
753
754
755
756
757
758
759
760
761
762
763
764
765
766
767
768
769
770
771
772
773
774
775
776
777
778
779
780
781
782
783
784
785
786
787
788
789

Correspondence and requests for materials should be addressed to I.A. or A.M.

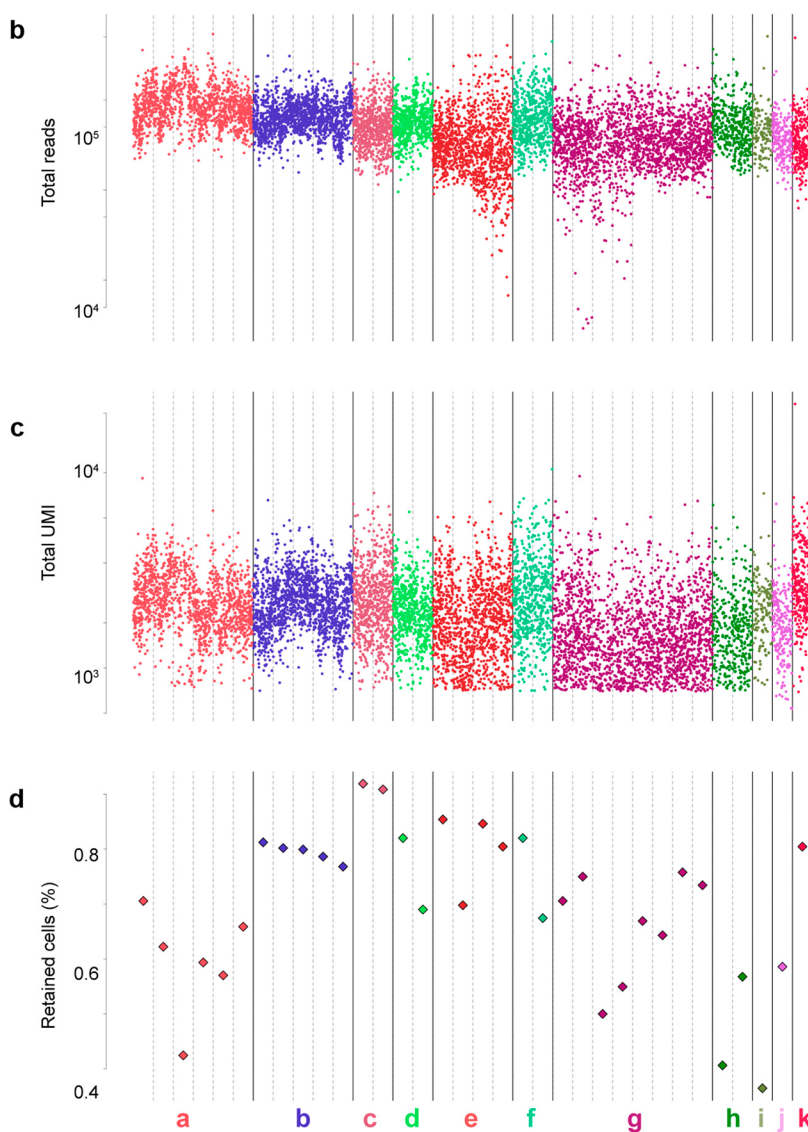
Peer review information Ioana Visan was the primary editor on this article and managed its editorial process and peer review in collaboration with the rest of the editorial team.

Reprints and permissions information is available at www.nature.com/reprints.

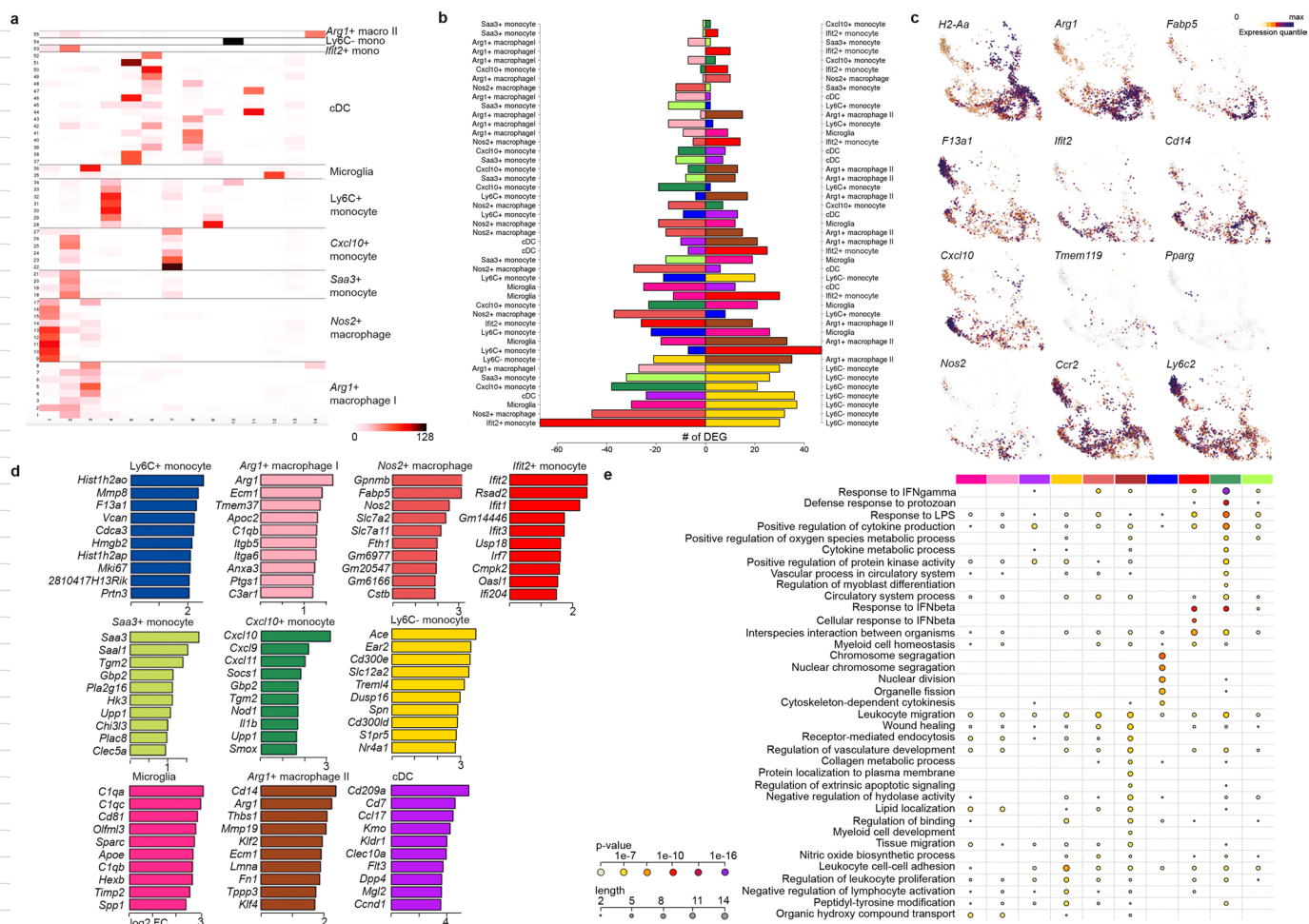
Uncorrected proofs

a

	EAE state	Gating	Experiment	nbatches	ncells
a	acute	Myeloid Gate		6	1373
b	chronic	Myeloid Gate		5	1524
c	acute	zbtb46-GFP+		2	702
d	chronic	zbtb46-GFP+		2	580
e	acute	Myeloid Gate	I	4	1230
f	acute	Myeloid Gate	II	2	574
g	acute	All CD45+ plus		8	2039
h	acute	transferred MDPs and monocytes		2	374
i	acute	transferred immunized monocytes		1	140
j	acute	transferred GMP		1	225
k	acute	transferred cMoP		1	309

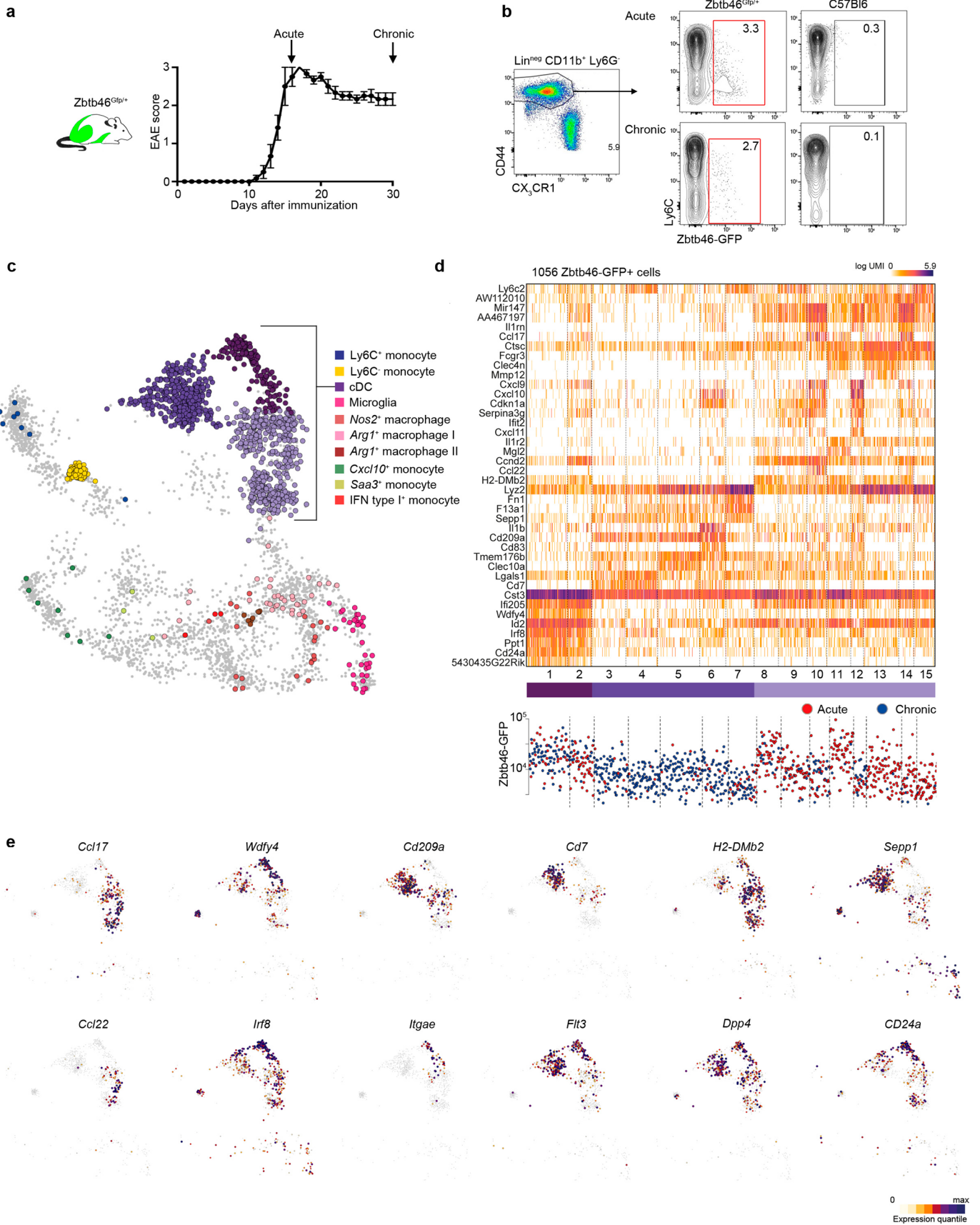


Extended Data Fig. 1 | Quality control of the scRNA-seq data. **a**, List of experiment and cell numbers used in this study. The number of cells represented here are numbers before exclusion of contaminating lymphocytes or neutrophils. **b**, Number of Illumina reads and **c**, total UMI per single cell. **d**, Fraction of analyzed cells after filtering. Cells are grouped and colored by experimental procedure.



Extended Data Fig. 2 | Identification of mononuclear phagocyte subsets in the inflamed CNS. a, Comparing Seurat and MetaCell clustering results. Rows represent the 55 identified metacells, grouped by their cell identity, and columns represent Seurat clusters. Color intensity in each entry depicts the number of cells assigned to a specific combination of MetaCells and Seurat clusters. **b**, Pairwise correlation analysis of the 10 distinct cell populations. Shown here are the numbers of differential expressed genes. **c**, Expression quantiles of key cell-type-specific marker genes on top of the 2D projection map. n = 2925 single cells were analyzed. **d**, Top 10 differentially expressed genes in each cluster (log₂ fold change). **e**, n = 2925 single cells were classified into the 10 indicated metacell subsets (color bar) and the top 60 differentially expressed genes were used for GO-enrichment of each cluster (these genes can be found in Supplementary Table 2). Circle color indicates p-value and size indicates number of genes. P-values indicate Benjamini Hochberg adjusted GSEA permutation tests.

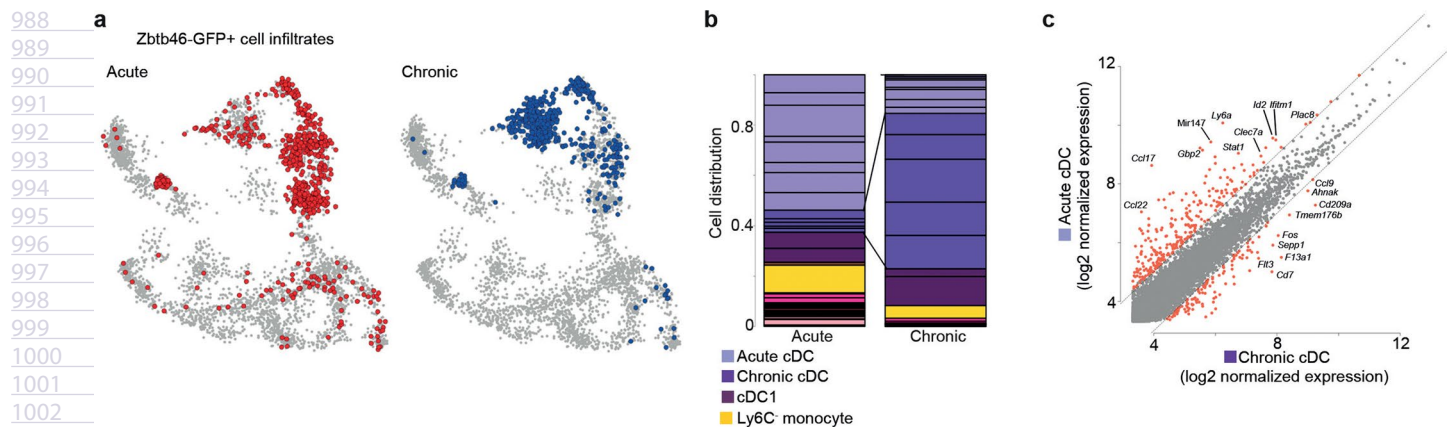
922
923
924
925
926
927
928
929
930
931
932
933
934
935
936
937
938
939
940
941
942
943
944
945
946
947
948
949
950
951
952
953
954
955
956
957
958
959
960
961
962
963
964
965
966
967
968
969
970
971
972
973
974
975
976
977
978
979
980
981
982
983
984
985
986
987



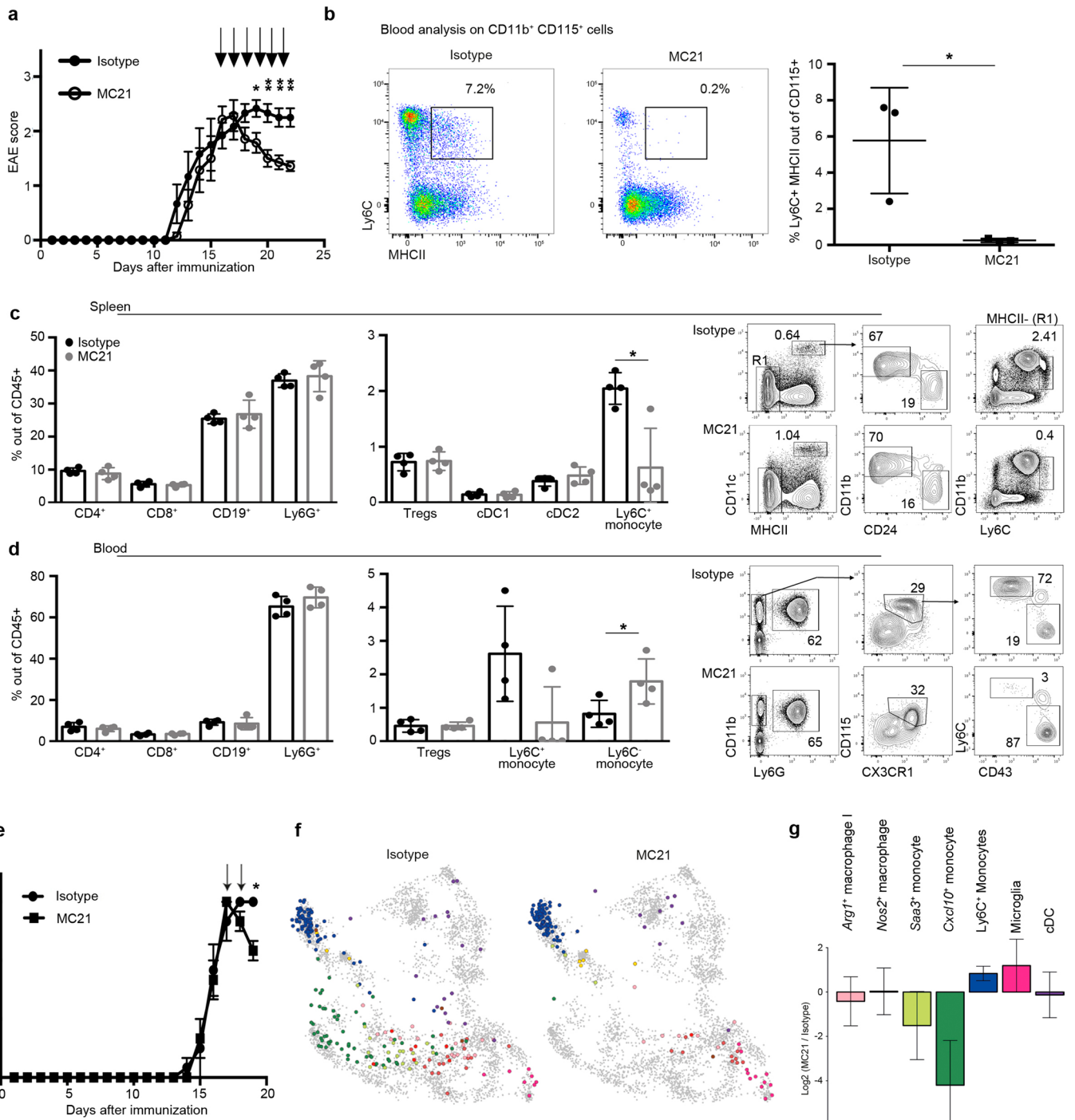
Extended Data Fig. 3 | See next page for caption.

Extended Data Fig. 3 | Characterization of dendritic cells in the inflamed CNS. **a**, EAE was induced in Zbtb46-GFP mice and cells were isolated from the inflamed spinal cord at the acute (day 15 p.i.; mean score: $2,7 \pm 0,4$ SEM; $n=6$) and the chronic phase (day 30 p.i.; mean score $2,2 \pm 0,4$ SEM; $n=7$). **b**, FACS analysis of $\text{Lin}^{\text{neg}}\text{Ly6G}^-\text{CD44}^{\text{high}}\text{CX}_3\text{CR1}^{\text{low-to-int}}\text{CD11b}^+$ cellular infiltrates into the spinal cord of acute (pool of $n=6$ mice) and chronic diseased EAE Zbtb46^{Gfp/+} mice (pool of $n=7$ mice). Shown is the gating for sorting GFP⁺ cells as indicated by the red square. **c**, Projection of 1282 Zbtb46-GFP⁺ cells on the 2D projection as shown in Fig. 1. **d**, Upper panel: Expression profiles of 1056 infiltrated Zbtb46-GFP⁺ cells that clustered into 15 DC metacells according to their transcriptomic similarities. Colorbar represent grouping of cells into three major cDC clusters. Dark violet correspond to cDC1 subset. Lower panel: MFI of Zbtb46-GFP expression in the sorted cells is shown on the bottom of the heatmap. Red dots indicate cells isolated during the acute phase, while blue dots indicate cells from the chronic phase. **e**, Expression quantiles of key cell-type-specific marker genes on top of the projection map. Single cell data represented in a-e are representative of one experiment.

Uncorrected proofs



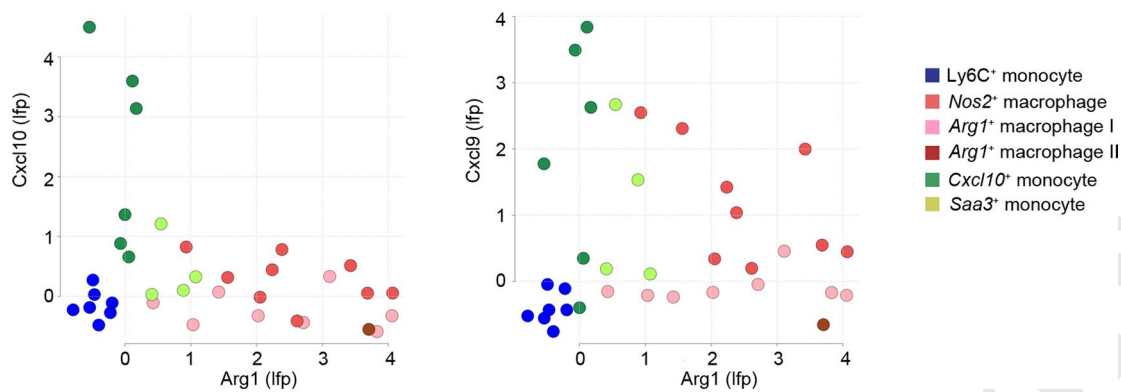
Extended Data Fig. 4 | Temporal resolution of cDC infiltrates in the acute and chronic stages of EAE. a, Projection of Zbtb46-GFP⁺ cells from Extended Data Fig. 3 separated according to the acute (left; pool of n = 6 mice) and chronic (right; pool of n = 7 mice) stage of EAE. n = 702 cells from acute and 580 from chronic disease stages were analyzed. **b**, Cell distribution of Zbtb46-GFP⁺ cells from both stages of disease. **c**, Differential gene expression between acute and chronic cDC. Values represent log-transformed normalized expression. Single cell data represented in a-c are representative of one experiment.



Extended Data Fig. 5 | See next page for caption.

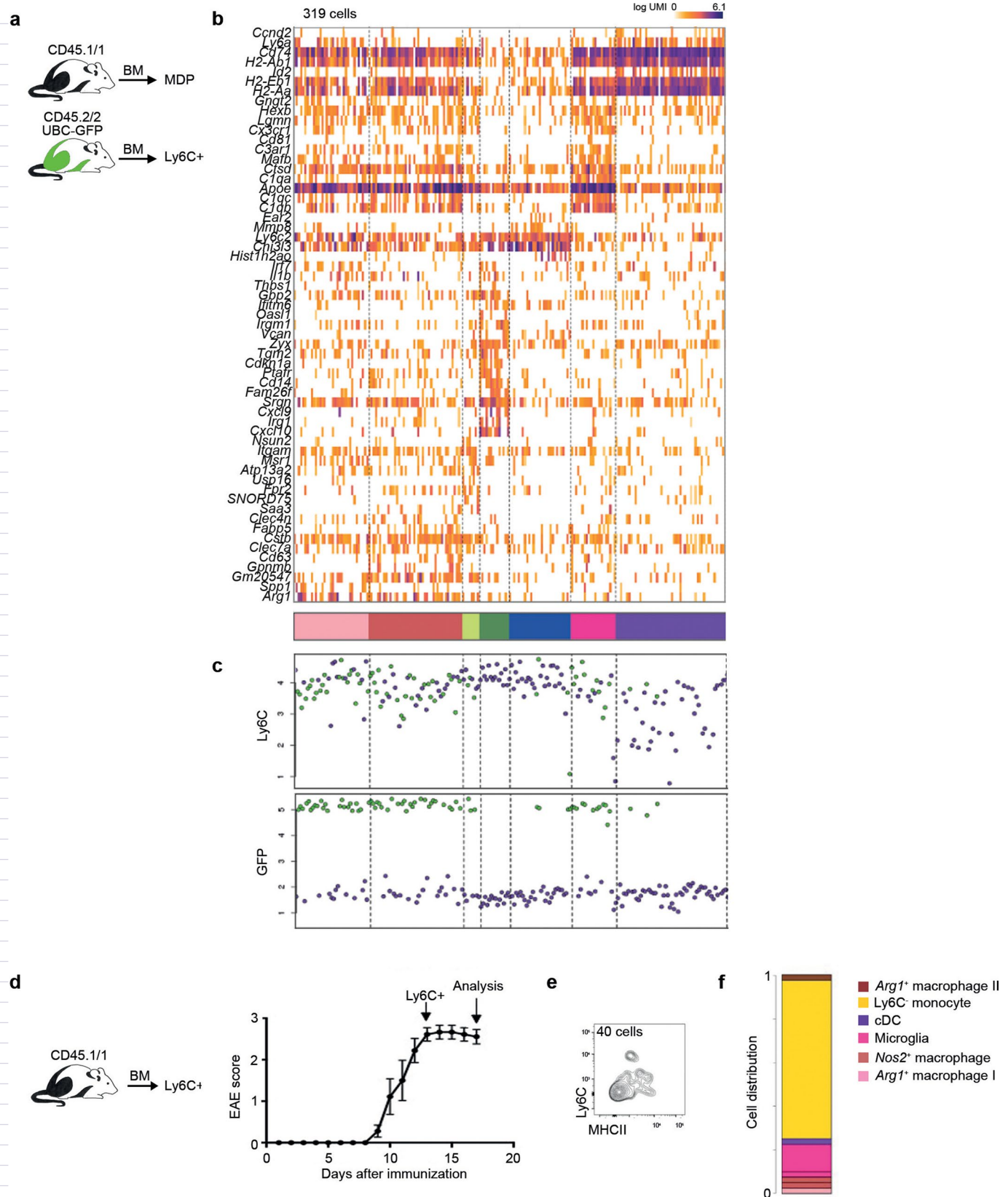
UNC

Extended Data Fig. 5 | Effects of MC21 depletion. **a**, Mice were immunized with MOG₃₅₋₅₅ and animals received at the peak of disease six injections of either 50 µg of isotype control antibody (rat IgG2b) or 50 µg purified anti-CCR2 (MC21). Shown is the mean clinical course ±SEM. N=6-7 mice per group and asterisk indicates statistical significance with * p < 0,05 and ** p < 0,005; unpaired two-tailed T-test. Data are representative of one experiment with six mice. **b**, FACS analysis (left) and quantification (right; mean ± SD) of Ly6C⁺ MHCII⁺ (IA^b) monocytes in the blood of isotype or MC21 treated mice. N=3 mice per group, asterisk indicates statistical significance with p < 0,05; unpaired two-tailed T-test. The experiment was repeated three times with similar results. **c**, Analysis and quantification of splenic immune cells in EAE mice that received two injections of 50 µg isotype control antibody or 50 µg purified anti-CCR2. Shown are % of the respective cell populations out of CD45⁺ cells (n=4 animals per group; experiment was performed twice with similar results; mean ± SD; asterisk indicates statistical significance with p < 0,01; unpaired two-tailed T-test). T_{regs} were identified as CD4⁺FoxP3⁺. **d**, Analysis and quantification of blood immune cells in EAE mice that received two injections of 50µg isotype control antibody or 50µg purified anti-CCR2 (MC21). Shown are % of the respective cell populations out of CD45⁺ cells (n=4 animals per group; experiment was performed twice with similar results; mean ± SD; asterisk indicates statistical significance with p < 0,05; unpaired two-tailed T-test). **e**, Repetition of Fig. 3 in an independent mouse facility and with purified MC21 antibody. Wt animals received either of 50µg isotype control antibody or 50µg purified anti-CCR2 at the peak of disease for two consecutive days. Shown are the EAE courses during the experiment (day 16 p.i., mean score in each group: isotype: 2.7 ± 0.3 SEM; MC21 3.0 ± 0.3 SEM; asterisk indicates statistical significance with p < 0,01; unpaired two-tailed T-test;). **f**, Projection of CD44⁺Ly6G⁻CD11b⁺ non-neutrophilic, non-microglial cells from isotype- (left) and MC21-treated (right) animals on the metacell model from Fig. 1. **g**, Bar plots showing enrichment (log₂ fold change) of myeloid groups in MC21-treated mice compared to isotype controls. Error bars represent 95% confidence intervals. 3 mice were pooled for MARS-seq analysis depicted in f,g and n=232 cells from isotype- and 147 cells from MC21-treated mice were analyzed in f, g.



Extended Data Fig. 6 | Expression of *Cxcl9* and *Cxcl10* in comparison to *Arg1*. Shown is the log₂ enrichment over median of *Cxcl9* and *Cxcl10* against *Arg1* in the main 6 monocyte clusters.

Uncorrected proof



Extended Data Fig. 7 | Identification of MDP and Ly6C⁺ derived cells in the CNS after sequential transfer. **a**, MDP were isolated from CD45.1/1 mice and BM Ly6C⁺ monocytes were extracted from Ubc-GFP mice as shown in Fig. 6a. **b**, Heatmap depicting gene expression across the transferred cells. **c**, Each cell was assigned to its GFP and Ly6C expression according to the indexed FACS measurement. Shown is the mean fluorescence intensity of each marker. **d**, 2×10^6 Ly6C⁺ monocytes were isolated from CD45.1/1 mice and transferred at the peak of disease into eight CD45.2/2 recipient mice (day 13 p.i.; mean clinical score \pm SEM are shown). **e**, 4 days after transfer, only 40 transferred cells could be re-isolated from the pooled spinal cord of recipients that showed no Ly6C and no MHCII expression. **f**, scRNA-seq identified that the majority of grafted cells show a Ly6C⁻ monocyte signature, while the remaining cells correspond to microglia-like cells and to Arg1⁺ subsets. Single cell data represented in d-f are representative of one experiment.

QUERY FORM

Nature Immunology	
Manuscript ID	[Art. Id: 661]
Author	Amir Giladi

AUTHOR:

The following queries have arisen during the editing of your manuscript. Please answer by making the requisite corrections directly in the e-proofing tool rather than marking them up on the PDF. This will ensure that your corrections are incorporated accurately and that your paper is published as quickly as possible.

Query No.	Nature of Query
Q1:	Since the references were not cited in numerical order, they have been renumbered in the order of appearance. Please check.
Q2:	Per style, genetic material is set in italics and gene products (including the mature forms of noncoding RNAs) are set upright. Please confirm that the italics/upright is appropriate or mark any instances that need to be changed.
Q3:	Your paper has been copy edited. Please review every sentence to ensure that it conveys your intended meaning; if changes are required, please provide further clarification rather than reverting to the original text. Please note that formatting (including hyphenation, Latin words, and any reference citations that might be mistaken for exponents) has been made consistent with our house style.
Q4:	Please ensure that genes are correctly distinguished from gene products: for genes, official gene symbols (e.g., NCBI Gene) for the relevant species should be used and italicized; gene products such as proteins and noncoding RNAs should not be italicized.
Q5:	Please check your article carefully, coordinate with any co-authors and enter all final edits clearly in the eproof, remembering to save frequently. Once corrections are submitted, we cannot routinely make further changes to the article.
Q6:	Note that the eproof should be amended in only one browser window at any one time; otherwise changes will be overwritten.
Q7:	Author surnames have been highlighted. Please check these carefully and adjust if the first name or surname is marked up incorrectly. Note that changes here will affect indexing of your article in public repositories such as PubMed. Also, carefully check the spelling and numbering of all author names and affiliations, and the corresponding email address(es).
Q8:	You cannot alter accepted Supplementary Information files except for critical changes to scientific content. If you do resupply any files, please also provide a brief (but complete) list of changes. If these are not considered scientific changes, any altered Supplementary files will not be used, only the originally accepted version will be published.
Q9:	We reserve 'significant' and its derivatives to mean statistically significant; for all instances in this paper, please re-word (e.g. 'important', 'notable', 'substantial') or supply a statistical measure such as P value. See the sentence beginning 'We detected a significant increase of Cxcl10+ monocytes during disease progression...' for the first use; in this instance, would 'notable' be OK?
Q10:	In the sentence beginning 'When analyzed at day 21 p.i, MC21-injected mice showed significant clinical im-

QUERY FORM

Nature Immunology	
Manuscript ID	[Art. Id: 661]
Author	Amir Giladi

AUTHOR:

The following queries have arisen during the editing of your manuscript. Please answer by making the requisite corrections directly in the e-proofing tool rather than marking them up on the PDF. This will ensure that your corrections are incorporated accurately and that your paper is published as quickly as possible.

Query No.	Nature of Query
	provement,' could 'significant' be changed to 'notable'?
Q11:	Please define scRNA-seq on its first use in text. Is this 'single-cell RNA-seq'?
Q12:	In the sentence beginning 'We did not observe significant changes to neutrophil levels' could 'significant' be changed to 'notable'?
Q13:	In the sentence 'MDPs from the bone marrow were MACS pre-enriched by antiCD135 biotin antibody' please spell out MACS
Q14:	Acknowledgements: Please check that all funders have been appropriately acknowledged and that all grant numbers are correct.
Q15:	Data availability: If applicable, please ensure accession codes are scheduled for release on or before this article's scheduled publication date, and update the database record with publication details from this article once available.
Q16:	Please check that the Competing Interests declaration is correct as stated. If you declare competing interests, please check the full text of the declaration for accuracy and completeness.

Reporting Summary

Nature Research wishes to improve the reproducibility of the work that we publish. This form provides structure for consistency and transparency in reporting. For further information on Nature Research policies, see [Authors & Referees](#) and the [Editorial Policy Checklist](#).

Statistics

For all statistical analyses, confirm that the following items are present in the figure legend, table legend, main text, or Methods section.

n/a Confirmed

- The exact sample size (n) for each experimental group/condition, given as a discrete number and unit of measurement
- A statement on whether measurements were taken from distinct samples or whether the same sample was measured repeatedly
- The statistical test(s) used AND whether they are one- or two-sided
Only common tests should be described solely by name; describe more complex techniques in the Methods section.
- A description of all covariates tested
- A description of any assumptions or corrections, such as tests of normality and adjustment for multiple comparisons
- A full description of the statistical parameters including central tendency (e.g. means) or other basic estimates (e.g. regression coefficient) AND variation (e.g. standard deviation) or associated estimates of uncertainty (e.g. confidence intervals)
- For null hypothesis testing, the test statistic (e.g. F , t , r) with confidence intervals, effect sizes, degrees of freedom and P value noted
Give P values as exact values whenever suitable.
- For Bayesian analysis, information on the choice of priors and Markov chain Monte Carlo settings
- For hierarchical and complex designs, identification of the appropriate level for tests and full reporting of outcomes
- Estimates of effect sizes (e.g. Cohen's d , Pearson's r), indicating how they were calculated

Our web collection on [statistics for biologists](#) contains articles on many of the points above.

Software and code

Policy information about [availability of computer code](#)

Data collection

No open-source or custom code was used to collect data for this paper

Data analysis

For FACS analysis, we used the following software: FACSDiva 7 FlowJo 10.4.2.
All subsequent bioinformatic data analysis was done in R, version 2.1 to 3.4. Data analysis was done with the custom made MetaCell package, which is available online (<https://bitbucket.org/tanaylab/metacell/src/default/>).

For manuscripts utilizing custom algorithms or software that are central to the research but not yet described in published literature, software must be made available to editors/reviewers. We strongly encourage code deposition in a community repository (e.g. GitHub). See the Nature Research [guidelines for submitting code & software](#) for further information.

Data

Policy information about [availability of data](#)

All manuscripts must include a [data availability statement](#). This statement should provide the following information, where applicable:

- Accession codes, unique identifiers, or web links for publicly available datasets
- A list of figures that have associated raw data
- A description of any restrictions on data availability

Data generated during this study have been deposited in Gene Expression Omnibus (GEO; GSE144317). Scripts and auxiliary data needed to reconstruct analysis files will be made available by request.

Field-specific reporting

Please select the one below that is the best fit for your research. If you are not sure, read the appropriate sections before making your selection.

Life sciences Behavioural & social sciences Ecological, evolutionary & environmental sciences

For a reference copy of the document with all sections, see [nature.com/documents/nr-reporting-summary-flat.pdf](https://www.nature.com/documents/nr-reporting-summary-flat.pdf)

Life sciences study design

All studies must disclose on these points even when the disclosure is negative.

Sample size	No statistical methods were used to predetermine sample size. Sample sizes for animal studies were made as large as possible based on the complex genetics. Number of sequenced single cells was determined to ensure detection of subpopulations and is on par with technical standards in the field. Single cells were collected from pools of 5-7 independent mice per experiment (Fig. 1-3). Experiments in Fig. 4+5 (and Suppl. Fig. 3) were performed with 3 mice per group. 6-10 mice were used as recipients in Figure 6. Figures 1,2,3 and 5 were repeated twice with similar results. Single cell data represented in Fig. 4 and 6 were performed once.
Data exclusions	Exclusion of single cells was done according to detection depth (less than 500 UMI per cell). Since we focused in this study on the analysis of cells belonging to the mononuclear phagocyte system, we excluded contaminating neutrophils and T cells, whose mean expression of S100a8 and Thy1, respectively, was strongly enriched over the median across meta-cells
Replication	All samples were done in biological and technical replicates as stated above ('Sample Size'). All replications yielded similar results.
Randomization	No randomization was done, since all animals used were isogenic mice or received a specific antibody treatment.
Blinding	No blinding was done, since the computational framework was identical for all processed animal samples.

Reporting for specific materials, systems and methods

We require information from authors about some types of materials, experimental systems and methods used in many studies. Here, indicate whether each material, system or method listed is relevant to your study. If you are not sure if a list item applies to your research, read the appropriate section before selecting a response.

Materials & experimental systems

n/a	Involved in the study
<input type="checkbox"/>	<input checked="" type="checkbox"/> Antibodies
<input checked="" type="checkbox"/>	<input type="checkbox"/> Eukaryotic cell lines
<input checked="" type="checkbox"/>	<input type="checkbox"/> Palaeontology
<input type="checkbox"/>	<input checked="" type="checkbox"/> Animals and other organisms
<input checked="" type="checkbox"/>	<input type="checkbox"/> Human research participants
<input checked="" type="checkbox"/>	<input type="checkbox"/> Clinical data

Methods

n/a	Involved in the study
<input checked="" type="checkbox"/>	<input type="checkbox"/> ChIP-seq
<input type="checkbox"/>	<input checked="" type="checkbox"/> Flow cytometry
<input checked="" type="checkbox"/>	<input type="checkbox"/> MRI-based neuroimaging

Antibodies

Antibodies used	All cells, except for GMP isolation, were blocked before staining with anti-CD16/32 (93; BioLegend: 101320; for stainings: 101307; dilution: 1:100) and antibodies against B220 (RA3-6B2; BioLegend: 103227; BD: 553092; dilution: 1:200), CD11b (M1/70; BioLegend: 101228; 101222; dilution: 1:200), CD11c (N418; BioLegend: 117318; 117322; dilution: 1:100), CD115 (AFS98; BioLegend: 135508; 135524; Invitrogen: 12-1152-82; dilution: 1:100), CD117 (2B8; BioLegend: 105803; 105847; 105812; dilution: 1:100), Ly6C (HK1.4; BioLegend: 128026; 128011; dilution: 1:200), CD135 (A2F10; BioLegend: 135308; 125309; 135305; dilution: 1:100), Ly6G (1A8; BioLegend: 127614; 127607; dilution: 1:200), TCRb (H57-597; BioLegend: 109230), TCRgd (GL3; BioLegend: 118120); CD4 (GK1.5; BioLegend: 100434, dilution: 1:100), CD45 (30-F11; BioLegend: 103112; BD: 559864; eBioscience: 83-0451-42; dilution: 1:100), CD45.1 (A20; BioLegend: 110714; dilution: 1:100), CD45.2 (1D4; BioLegend: 109808; dilution: 1:100), CD8a (53-6.7; BD: 553030; dilution: 1:200), NK1.1 (PK136; BioLegend: 108741; dilution: 1:100), I-Ab (MHCI; AF6-120.1; eBioscience: 11-5320-82; Invitrogen: 12-5320-82; dilution: 1:200), CX3CR1 (SA011F11; BioLegend: 149016; dilution: 1:100), CD34 (HM34; BioLegend: 128607; dilution: 1:100), FoxP3 (FJK-16s; Invitrogen: 12-5773-80; dilution: 1:100), CXCL9 (MIG-2F5.5; BioLegend: 515603; dilution: 1:100), Arginase (A1exF5; eBioscience: 25-3697-80; dilution: 1:100), CD44 (IM7; BioLegend: 103040; dilution: 1:100), CD24 (M1/69; BioLegend: 101813; dilution: 1:100), CD43 (S7; BD: 553271; dilution: 1:200) and CD103 (2E7; BioLegend: 121405; dilution: 1:100) were used. For CXCL9 and Arginase stainings, Percoll-isolated mononuclear infiltrates were incubated in full RPMI media supplemented with 1x Brefeldin A at 37°C for 3 hours. Intracellular stainings were performed with the Biolegend FoxP3 fix/perm kit. from Biolegend or eBioscience were used. CCR2 (MC21) and isotype control (rat IgG2b) antibody was provided by Matthias Mack
Validation	All antibodies against surface-expressed markers used in this study have been previously validated by the manufacturer, as

stated on their associated product webpages, and by our own lab in previous experiments. In case of new markers, such as CXCL9 and Arginase, we confirmed antibody specificity by Isotype control stainings (as shown in Fig. 5c)

Animals and other organisms

Policy information about [studies involving animals](#); [ARRIVE guidelines](#) recommended for reporting animal research

Laboratory animals	6-12 week-old female mice were used in this study. The following strains were used: C57BL/6 mice Zbtb46Gfp/+ mice (B6.129S6(C)-Zbtb46tm1.1Kmm/J) Ubiquitin-GFP mice (C57BL/6-Tg(UBC-GFP)30Scha/J) CD45.1/1 mice (B6.SJL-PtprcaPep3b/BoyJ)
Wild animals	No wild animals used.
Field-collected samples	No field-collected samples used.
Ethics oversight	All animal experiments have been approved by the LAGeSo in Berlin or by the Weizmann Institute Animal Care Committee (IACUC) in accordance with international guidelines.

Note that full information on the approval of the study protocol must also be provided in the manuscript.

Flow Cytometry

Plots

Confirm that:

- The axis labels state the marker and fluorochrome used (e.g. CD4-FITC).
- The axis scales are clearly visible. Include numbers along axes only for bottom left plot of group (a 'group' is an analysis of identical markers).
- All plots are contour plots with outliers or pseudocolor plots.
- A numerical value for number of cells or percentage (with statistics) is provided.

Methodology

Sample preparation	For peripheral blood analysis, blood was collected and mononuclear cells were enriched by Ficoll density gradient centrifugation (2200rpm, 15 min at 20°C with low acceleration and no brake). For CNS analysis mice were perfused with 5 ml PBS via the left ventricle and spinal cord samples were harvested from individual mice. Meninges were removed. CNS tissues were cut into small pieces and homogenized through a 100µm mesh filter without tissue digestion. After washing (2000rpm, 5min, 14°C), the cell pellet was resuspended in 40% Percoll and the myelin fraction was separated from mononuclear cells by density centrifugation (2200rpm, 20 min at 14°C with low acceleration and no brake). MDP from the BM were MACS pre-enriched by anti-CD135 biotin antibody followed by anti-biotin microbeads (Miltenyi). Ly6C+ monocytes from the spleen or BM were pre-enriched by anti-CD115 biotin antibody followed by anti-biotin microbeads (Miltenyi). All cells were blocked before staining with anti-CD16/32 (93). GMP from the BM were enriched with anti-CD117 antibody followed by anti-biotin microbeads (Miltenyi).
Instrument	Samples were flow sorted either using ArialI, ArialII or Aria-Fusion (BD Biosciences, BD Diva Software) cell sorter. Analysis was performed on Fortessa or LSRII (BD Biosciences, BD Diva Software)
Software	FACS was operated with FACSDiva 7 FACS data was analyzed with FlowJo 10.4.2. Index sorting data was read via the Bioconductor package flowCore and analyzed using custom code, available at the Git repository (https://bitbucket.org/tanaylab/hematopoiesis2018).
Cell population abundance	The sorting efficiency is mentioned where applicable.
Gating strategy	Cells were first gated according to their FSC-A/SSC-A behavior. Singlets were identified by FSC-A/FSC-H. CD11b+ and CD45+ were gated, and cells were excluded that were positive for the neutrophilic marker Ly6G. Afterwards, microglia were excluded through their CX3CR1hi CD44low phenotype. The complete gating strategy is shown in Fig 1b.

- Tick this box to confirm that a figure exemplifying the gating strategy is provided in the Supplementary Information.